1 **Revision 2**

2 **A comparison of olivine-melt thermometers based on D_{Mg} and D_{Ni}: the**

3 **effects of melt composition, temperature and pressure with applications**

4 **to MORBs and hydrous arc basalts**

5

6 Xiaofei Pu, Rebecca A. Lange, Gordon Moore

7 Department of Earth and Environmental Sciences

8 University of Michigan

9 Ann Arbor, MI 48109-1005

10 Corresponding author email: pux@umich.edu

11

12 **ABSTRACT**

13 A new olivine-melt thermometer based on the partitioning of Ni ($D_{Ni}^{oliv/liq}$), with a

14 form similar to the Beattie (1993) $D_{Mg}^{oliv/liq}$ thermometer, is presented in this study. It is

15 calibrated on a dataset of 123 olivine-melt equilibrium experiments from 16 studies in the

16 literature that pass the following five filters: (1) 1-bar only, (2) analyzed totals between

17 99.0-101.0 wt% for olivine and 98.5-101.0 wt% for quenched glasses, (3) olivine is the

18 only silicate phase in equilibrium with the melt, (4) the NiO concentration is ≥ 0.1 wt% in

19 olivine and ≥ 0.01 wt% in quenched glass, and (5) no metallic phase is present other than

20 the capsule. The final dataset spans a wide range of temperature (1170-1650 °C), liquid

21 composition (37-66 wt% SiO_2; 4-40 wt% MgO; 107-11087 ppm Ni), and olivine

22 composition (Fo_{36-100}; 0.10-15.7 wt% NiO). The Ni-thermometer recovers the 123

23 experimental temperatures within $\pm$ 29 °C (1σ), with an average residual of 0 °C. A re-

1

24   fitted version of the Mg-thermometer of Beattie (1993), calibrated on the same 123

25   experiments as for the Ni-thermometer, results in an average residual of 1 ± 26 °C (1σ).

26   When both thermometers are applied to the same 123 experiments, the average ΔT (T_{Mg}-

27   T_{Ni}) is 1 ± 29°C (1σ), which confirms that the Mg- and Ni-thermometers perform equally

28   well over a wide range of anhydrous melt composition and temperature at 1 bar. The

29   pressure dependence of the Ni-thermometer under crustal conditions (≤ 1 GPa) is shown

30   to be negligible through comparison with experimental results from Matzen et al. (2013),

31   whereas the pressure dependence of the Mg-thermometer is up to 52°C at ≤ 1 GPa

32   (Herzberg and O'Hara, 2002). Therefore, neglecting the effect of pressure when

33   applying both thermometers to basalts that crystallized olivine at crustal depths (≤ 1 GPa)

34   is expected to lead to negative ΔT (T_{Mg}-T_{Ni}) values ($\leq$ -52 °C). Application of the two

35   thermometers to nine mid-ocean ridge basalts results in an average ΔT of -3 degrees,

36   consistent with shallow crystallization of olivine under nearly anhydrous conditions. In

37   contrast, application of the two thermometers to 18 subduction-zone basalts leads to an

38   average ΔT of +112 degrees; this large positive ΔT value cannot be explained by the

39   effect of pressure, temperature or anhydrous melt composition. It is well documented in

40   the literature that $D_{Mg}^{oliv/liq}$ is affected by dissolved water in the melt and that Mg-

41   thermometers overestimate the temperature of hydrous basalts if an H_2O correction is not

42   applied (e.g., Putirka et al., 2007). Therefore, the reason why hydrous arc basalts have

43   higher ΔT (T_{Mg}-T_{Ni}) values than MORBs may be because $D_{Ni}^{oliv/liq}$ is less sensitivite to

44   water in the melt, which is supported by new Ni-partitioning results on three olivine-melt

45   equilibrium experiments on a basaltic andesite with up to 5 wt% H_2O. More hydrous

46   experiments are needed to confirm that the Ni-thermometer can be applied to hydrous

47   melts without a correction for H_2O in the melt.

48

49   **INTRODUCTION**

50   The importance of obtaining the magmatic temperatures of basalts has long been

51   recognized and pursued by Earth scientists. Numerous researchers have mapped global

52   variations in mantle temperature by applying olivine-melt thermometers based on Mg-

53   partitioning ($D_{Mg}^{oliv/liq}$) to basalts from mid-ocean spreading ridges (e.g. Falloon et al.,

54   2007; Genske et al., 2012) and the Iceland and Hawaiian plumes (e.g. Neave et al., 2015;

55   Xu et al., 2014). These efforts not only constrain conditions for mantle melting at

56   different tectonic settings, including depth of melting (e.g., Lee et al., 2009) and thermal

57   anomalies associated with mantle plumes (e.g., Herzberg et al., 2007; Falloon et al., 2007;

58   Putirka et al., 2007), but also have contributed substantially to our understanding of how

59   the Earth's mantle has cooled through time (e.g., Herzberg and Gazel, 2009).

60   The reliability of these results largely depends on the accuracy of applied olivine-

61   melt thermometers. There is general agreement (e.g., Herzberg et al., 2007; Falloon et al.,

62   2007; Putirka, 2008; Herzberg and Asimow, 2015) that the Beattie (1993) form of the

63   thermometer recovers experimental temperatures the best under anhydrous conditions

64   (e.g., standard error estimate of $\pm$ 44°C; Putirka, 2008) and produces temperatures similar

65   to the model of Ford et al. (1983) and those obtained by the MELTS program (Ghiorso

66   and Sack, 1995; Asimow et al., 2001) for anhydrous natural samples. When applied to

67   hydrous liquids, however, all thermometers based on $D_{Mg}^{oliv/liq}$ (e.g., Ford et al., 1983;

68   Beattie, 1993), require a major correction for the dissolved H_2O content when applied to

69   hydrous liquids, possibly because hydroxyl groups complex with Mg^{2+} to lower its

                                                                                         3

70   activity in hydrous melts (e.g., Waters and Lange, 2013). Putirka et al. (2007) provides a

71   modified thermometer (Eq. 4 in that study) that includes an H_2O term, which reproduces

72   experimental temperatures with a high overall precision (standard error estimate of 29˚C;

73   Putirka, 2008). Thus, the application of any currently available olivine-melt thermometer

74   based on Mg-partitioning to hydrous basalts requires that melt H_2O concentration be

75   known a priori.

76   In this study, the potential of a new olivine-melt thermometer based on the

77   partitioning of Ni ($D_{Ni}^{oliv/liq}$) is evaluated in comparison to the best available $D_{Mg}^{oliv/liq}$

78   thermometer as a function of anhydrous melt composition, temperature and pressure

79   through a common set of phase-equilibrium experiments from the literature.   Both the

80    $D_{Ni}^{oliv/liq}$ and $D_{Mg}^{oliv/liq}$ thermometers are applied to a set of nine mid-ocean ridge basalts

81   (MORBs) and 18 subduction-zone basalts to test whether there is any difference in the

82   results for samples that are relatively anhydrous (i.e., MORBs) vs. hydrous (i.e., arc

83   basalts). In light of the large systematic difference in the Ni- and Mg-thermometers for

84   arc basalts, but not for MORBs, new Ni-partitioning results for olivine-melt equilibrium

85   experiments on a hydrous basaltic andesite are presented to test the relative sensitivity of

86    $D_{Ni}^{oliv/liq}$ and $D_{Mg}^{oliv/liq}$ to up to 5 wt% H_2O in the melt phase.

87

88   **ANALYTICAL METHODS**

89   Olivine compositions were measured with a five-spectrometer Cameca SX-100

90   electron microprobe at the University of Michigan. The analyses were made with a

91   focused beam, with an acceleration voltage of 15kV and a beam current of 20nA. Eight

92   elements were measured (Mg, Fe, Si, Ni, Al, Mn, Cr, Ca).   The peak and background

4

93   counting times were 30s each for Si, Mg, Fe and Ni, and 20 s each for Al, Mn, Cr and Ca.

94   The 1σ precision based on counting statistics is $\pm$ 0.32 wt% SiO_2, $\pm$ 0.25 wt% MgO, $\pm$

95   0.54 wt% FeO, and $\pm$ 0.05 wt% NiO, and < 0.1 wt% for Cr_2O_3, Al_2O_3, MnO and CaO.

96   The standards used for all analyses are from the University of Michigan collection for the

97   electron microprobe and are described in Appendix A.   Oxygen was calculated by cation

98   stoichiometry and used in the Cameca PAP correction program. Traverses across 20-30

99   olivine crystals were conducted in all natural samples. Traverses along the darker (Mg-

100   rich) region on the back-scattered electron (BSE) image of each crystal were made, with

101   an analysis every 20-30 μm, leading to approximately 200-500 effective olivine analyses

102   for each sample. Plagioclase crystals in two natural samples (UR-60, UR-61) were also

103   analyzed using the Cameca SX-100, but in this case seven elements were analyzed (Si,

104   Al, Fe, Ca, Na, K, Ba) using an accelerating voltage of 15 kV and a focused beam current

105   of 4 nA. The peak and background counting times were 30s each for all elements. The

106   1σ precision based on counting statistics is < 2% for SiO_2 and Al_2O_3, < 4% for CaO, and

107   < 5% for Na_2O. Traverse analyses across plagioclase phenocrysts were performed in the

108   same way as for olivine phenocrysts.

109   The Ni concentrations (ppm) in the quenched glass of experimental run products

110   were analyzed by laser ablation using a Photon Machines Analyte G2 193 nm Ar-F

111   excimer laser coupled with a Thermo Scientific X series 2 Quadrapole inductively

112   coupled plasma mass spectrometer (ICP-MS) at Oregon State University. The beam size

113   was 50 μm and the counting time was 30s. GSE-1G was used as the reference standard

114   while monitoring standards BCR-2G and TI-G. The Ni content of the glass was

115   calculated relative to the reference standard GSE-1G, which was measured under

116   identical conditions throughout the same analytical session. To reduce the matrix effect,

117   ^{43}Ca was used as an internal standard, in conjunction with the CaO contents in the

118   experimental glasses, which were measured independently with an electron microprobe

119   and reported in Moore and Carmichael (1998). The 1σ uncertainty is 8%, which includes

120   the error from the reference standard GSE-1G. The procedures and protocols that were

121   followed are described more fully in Kent et al. (2004).

122

123   **OLIVINE-MELT THERMOMETRY**

124   **An olivine-melt thermometer based on Ni partitioning at 1 bar**

125   Nickel partitioning between olivine and basaltic melts has been extensively

126   studied as a function of anhydrous melt composition, temperature, and pressure by a large

127   number of researchers. Here, attention is first focused on the effect of anhydrous melt

128   composition and temperature on the partition coefficient for Ni between olivine and melt

129   ($D_{Ni}^{oliv/liq}$) at 1 bar; the effect of pressure is evaluated separately in another section below.

130   On the basis of nine experimental studies published over the last four decades (Arndt,

131   1977; Hart and Davis, 1978; Leeman and Lundstrom, 1978; Agee and Walker, 1990;

132   Kelemen et al., 1998; Wang and Gaetani, 2008; Li and Ripley, 2010; Putirka et al., 2011;

133   Matzen et al., 2013) thirteen different models were proposed to describe $D_{Ni}^{oliv/liq}$ as a

134   function of temperature and melt composition (Table 1).

135   To test the relative effectiveness of these different model equations at 1-bar, an

136   initial dataset of 328 1-bar experiments were compiled, which includes those that were

137   used to calibrate the Matzen et al. (2013) and Li and Ripley (2010) models, as well those

138   in the Library of Experimental Phase Relations (LEPR) (Hirschmann et al., 2008). Four

6

139   filters were then applied: (1) analyzed totals of olivine between 99.0-101.0 wt% and of

140   glass between 98.5-101.0 wt%; (2) olivine is the only silicate phase in equilibrium with

141   the melt; (3) the NiO concentration is ≥ 0.1 wt% in olivine and ≥ 0.1 wt% in quenched

142   glass (given the detection limits of the electron microprobe used to analyze the Ni

143   contents in both phases); (4) no metallic phase is present other than the capsule. The

144   purpose of these four filters is to exclude experiments where analytical uncertainties may

145   have been too high and/or where equilibrium may not have been attained among several

146   phases in crystal-rich experiments. Although some experiments that had small analytical

147   uncertainties and/or achieved equilibrium may have been excluded, the uniform

148   application of all four filters allowed a high-quality dataset to be compiled in an unbiased

149   manner. The final dataset includes 123 olivine-melt experiments at 1 bar from 16 studies

150   (Bird, 1971; Arndt, 1977; Takahashi, 1978; Nabelek, 1980; Kinzler et al., 1990; Ehlers et

151   al., 1992; Snyder and Carmichael, 1992; Jurewicz et al., 1993; Parman et al., 1997;

152   Gaetani and Grove, 1997; Tuff et al., 2005; Mysen, 2006; Mysen, 2007a; Mysen, 2007b;

153   Mysen, 2008; Wang and Gaetani, 2008; Matzen et al., 2013). The final dataset (compiled

154   in Appendix B) spans a wide range of liquid composition (37-66 wt% SiO_2; 4-40 wt%

155   MgO; 107-11087 ppm Ni), olivine composition (Fo_{36-100}; 0.13-15.7 wt% NiO), and

156   temperature (1170-1650 °C).

157   The thirteen $D_{Ni}^{oliv/liq}$ models in Table 1 were used to calculate temperature for the

158   123 experiments in Appendix B. Plots of the temperature residuals for each model are

159   shown in Appendix C (supplementary material). Among the thirteen models, the one

160   presented in Li and Ripley (2010) yields the best result with an average residual of -9 $\pm$

161   30°C (1σ), while the others have 1σ residuals that range from $\pm$ 54 to $\pm$119°C (Table 1;

7

162   Appendix C). Although the most recently published model of Matzen et al. (2013) has an

163   average residual of only 19 °C, the 1σ standard deviation is ± 98°C (Table 1; Appendix

164   C). Note that the Ni-partitioning experiments conducted by Matzen et al. (2013) are of

165   the highest quality, and both the Li and Ripley model (2010) and the Matzen et al. (2013)

166   models recovers the two 1-bar experiments from Matzen et al. (2013) within 22 and 35

167   °C, respectively.

168   The next step is to recalibrate all of the $D_{Ni}^{oliv/liq}$ thermometers in Table 1, using

169   the dataset of 123 olivine-melt experiments in Appendix B. The 13 models in Table 1

170   can be reduced to eight different forms of model equations, and the results of those re-

171   calibrations are shown in Table 2 and Appendix D (plots of the temperature residuals for

172   each model). The effect of recalibrating the model equations in Table 2 with 10000/T as

173   the dependent variable (instead of $lnD_{Ni}^{oliv/liq}$) leads to temperature-dependent residuals

174   (Appendices E and F) and is therefore not recommended.

175   The best model in Table 2 is obtained from the equation used by Li and Ripley

176   (2010), which is based on the simplified thermodynamic formulation of Beattie et al.

177   (1991) where the effect of melt composition (and polymerization) is modeled through the

178   term, $X_{Div}^{melt} / X_{SiO_2}^{melt}$, where X_{Div}^{melt} is equal to $X_{MgO}^{melt} + X_{FeO}^{melt} + X_{CaO}^{melt} + X_{MnO}^{melt} + X_{CoO}^{melt} + X_{NiO}^{melt}$ and

179    $X_{SiO_2}^{melt}$ is the mole fraction of SiO₂ in the melt. To first order, this compositional term

180   tracks the degree of melt polymerization, which has been shown to increase the value of

181    $D_{Ni}^{oliv/liq}$ (e.g., Hart and Davis, 1978; Wang and Gaetani, 2008). Interestingly, this

182   simplified compositional parameter leads to a better model equation than one that is

183   based on the parameter NBO/T (non-bridging oxygens over tetrahedral units), which was

184   introduced by Mysen et al. (1985) to model the degree of melt polymerization. The

8

185   NBO/T parameter is included in Model D (Table 2), the form used by Wang and Gaetani

186   (2008), and results in a higher 1σ standard deviation ($\pm$ 60 °C) than that ($\pm$ 31 °C) for the

187   Li and Ripley (2010) form (Model A in Table 2) when calibrated on the 123 1-bar

188   experiments.

189   A final model equation for the Ni-thermometer is based on the general form of the

190   Beattie (1993) Mg-thermometer. In this empirical version (Eq. 1), $D_{Ni}^{oliv/liq}$ is substituted

191   for $D_{Mg}^{oliv/liq}$ (both constructed on a molar basis) and the coefficients in front of the

192   molar compositional terms are fitted parameters. In this equation, the effect of melt

193   polymerization is incorporated with the combined terms X_{NM} and X_{SiO2}, which are

194   defined below. Although the original Beattie (1993) model equation uses cation fractions

195   instead of mole fractions, the results of a calibration on the 123 experiments in Appendix

196   B have lower residuals if mole fractions are used. The generalized form of the equation

197   is given here:

$$\ln D_i^{ol/melt} = a + \frac{b}{T} + c\ln\left(X_{NM}^{liq}\right) + d\ln\left(X_{SiO_2}^{liq}\right) + e(NF) \tag{1}$$

199   where T is in Kelvin, $X_{NM}^{liq} = X_{FeO}^{liq} + X_{MgO}^{liq} + X_{MnO}^{liq} + X_{CaO}^{liq} + X_{CoO}^{liq} + X_{NiO}^{liq}$ (mole fraction

200   components), $X_{SiO_2}^{liq}$ is the mole fraction of SiO_2 in the melt, and NF =

201    $3.5\ln\left(1 - X_{Al_2O_3}\right) + 7\ln\left(1 - X_{TiO_2}\right)$. The results of the calibration of Equation 1 (for i=Ni) on

202   the 123 experiments in Appendix B are given in Table 3, with residuals plotted in Figure

203   1a. This model provides the best overall fit to the data, with an average residual of 0 $\pm$

204   29°C and a R^2 of 0.96, and it is the Ni-thermometer recommended in this study (Table 3).

205

206   **An updated olivine-melt thermometer based on Mg partitioning at 1 bar**

207   Since the publication of the landmark study by Roeder and Emslie (1970),

208   numerous geothermometers based on the partitioning of Mg between olivine and silicate

209   melt have been proposed. In a review of olivine-melt thermometers, Putirka (2008)

210   showed that the general form of the Beattie (1993) model (Eq.1) leads to the most

211   accurate results. When the Beattie (1993) and Putirka et al. (2007) Mg-thermometers are

212   applied to the 123 olivine-melt 1-bar experiments in Appendix B (used to calibrate the

213   Ni-thermometer in Eq. 1), the average residuals are 17 ± 30 (1σ) and 0 ± 31 (1σ),

214   respectively (Table 4; Appendix G). Here, we perform a re-calibration of the general

215   form of the Beattie (1993) Mg-thermometer on the 123 experiments in Appendix B, using

216   the empirical form shown in Equation 1.   The results of the regression are given in Table

217   3, with residuals plotted in Figure 1b.   This model provides an excellent fit to the 123

218   olivine-melt experiments, with an average residual of 1 ± 26°C and a R^2 of 0.96, and it is

219   the Mg-thermometer recommended in this study.

220

221   **A comparison of the Ni- and Mg-thermometers at 1 bar**

222   In order to directly compare the results of the Ni-thermometer (T_{Ni}) with those of

223   the Mg-thermometer (T_{Mg}) on the 123 experiments, a parameter ΔT ($= T_{Mg} - T_{Ni}$) was

224   constructed for this dataset. A plot of ΔT as a function of experimental temperature is

225   shown in Figure 1c; the average ΔT is 1 ± 29°C (1σ). This result confirms that the Ni-

226   thermometer and the Mg-thermometer (Table 3, Eq. 1) perform equally well over a wide

227   range of anhydrous melt composition ($SiO_2 = 37$-66 wt%; $MgO = 4$-40 wt%) and

228   temperature (1160-1650 °C) at 1 bar. Therefore, if the two thermometers are applied to a

229   series of basalts that crystallized at shallow depths and contained little dissolved H_2O

10

230   (e.g., MORBs), ΔT (= $T_{Mg} - T_{Ni}$) is expected to be close to zero. A test of whether or not

231   this is the case is presented below in an application to mid-ocean ridge basalts, but first

232   the effect of pressure on both the Mg- and Ni-thermometers is evaluated.

233

234   **The effect of pressure on the Mg- and Ni-thermometers**

235   Herzberg and O'Hara (2002) examined the effect of pressure on the Beattie

236   (1993) $D_{Mg}^{oliv/liq}$ thermometer and proposed the following pressure correction:

237                    $T(P) = T_{1\text{-}bar} + 54P(GPa) - 2P(GPa)^2$ (2)

238   This pressure correction can be tested against the high-quality experimental results of

239   Matzen et al. (2013), where olivine-melt equilibrium experiments were performed on a

240   MORB sample between 1 bar and 3 GPa. Application of the updated Mg-thermometer

241   (Table 3, Eq. 1) to the Matzen et al. (2013) experiments allows the residuals ($T_{experimental}$ -

242   T_{Mg}) to be plotted as a function of pressure. In Figure 2, the solid curve shows the

243   Herzberg and O'Hara (2002) pressure correction (Eq. 2), which agrees well with the

244   Matzen experiments.

245   The exchange of Mg between olivine and liquid can be described by the following

246   reaction:

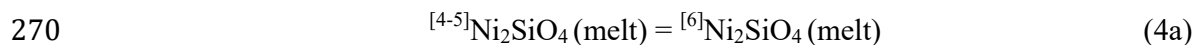247 Mg_2SiO_4 (melt) = Mg_2SiO_4 (olivine),   (3)
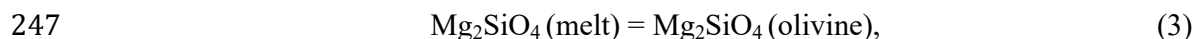
248   In Equation 3, the lower volume (olivine) side of the reaction is favored with higher

249   pressure. Therefore, increasing pressure (while holding all other parameters constant)

250   will result in higher $D_{Mg}^{oliv/liq}$ values, which leads to lower calculated temperatures (Eq.

251   1). Thus, the effect of not including a pressure correction to the Mg-thermometer will

11

252   lead to underestimates of temperature (by $\leq 52°C$ for melts that crystallize olivine at ≤ 1

253   GPa, according to Eq. 2).

254   The Matzen et al. (2013) experiments can also be used to evaluate the pressure

255   dependence to $D_{Ni}^{oliv/liq}$. In this case, application of the Ni-thermometer (Table 3, Eq. 1)

256   leads to residuals (T_{expt} - T_{Ni}) that show a step-like distribution with pressure, with little

257   dependence between 1 bar and 1 GPa, and then a marked pressure dependence between 2

258   and 3 GPa. At 1 bar, the two Matzen et al. (2013) experiments have residuals of -2 and -

259   9 degrees. At 1 GPa, the five Matzen et al. (2013) experiments all give a similar result,

260   with an average residual of -2 $\pm$ 6 °C. A linear fit to all seven residuals (dashed line in

261   Fig. 2) leads to an increase of only 4°C between 0 and 1 GPa.

262   A plausible explanation for the step-like behavior in Figure 2 is related to the

263   coordination of Ni^{2+} in the melt as a function of pressure. X-ray Absorption Near-Edge

264   Structure (XANES) spectroscopy shows that Ni^{2+} in silicate liquids is largely in 4- and 5-

265   fold coordination over a range of melt composition at 1 bar (Galoisy and Calas, 1993).

266   Moreover, Ni^{2+} is not abundant in 6-fold coordination at depths ≤ 1 GPa, but does

267   undergo a complete conversion to octahedral coordination by 4 GPa (Jones et al., 2011).

268   Therefore, we suggest two reactions to describe the effect of pressure on the Ni_2SiO_4

269   liquid component:

$$^{[4-5]}Ni_2SiO_4 \, (melt) = {}^{[6]}Ni_2SiO_4 \, (melt) \tag{4a}$$

$$^{[6]}Ni_2SiO_4 \, (melt) = {}^{[6]}Ni_2SiO_4 \, (crystal) \tag{4b}$$

272   At crustal pressures (<1 GPa), the predominant effect of increasing pressure is expressed

273   by the reaction in Equation 4a, where 4- and 5-fold coordinated Ni^{2+} in the melt is

12

274   gradually converted to 6-fold coordinated Ni^{2+}, whereas once 6-fold Ni^{2+} is abundant (≥ 2

275   GPa), the predominant effect of pressure is shown by the reaction in Equation 4b.

276   In contrast to the case for Ni^{2+}, evidence from nuclear magnetic resonance (NMR)

277   spectroscopy show that CaO-MgO-Al_2O_3-SiO_2 (CMAS) liquids (model basalts) at one

278   bar contain Mg^{2+} with an average coordination that is close to 6-fold, with minor amounts

279   that are 5-fold (George and Stebbins, 1998). This result is consistent with density

280   measurements on CaO-MgO-FeO-Al_2O_3-SiO_2 liquids, including $CaMgSi_2O_6$ (diopside)

281   and $CaFeSi_2O_6$ (hedenbergite) liquids, that result in partial molar volumes for CaO, MgO

282   and FeO at 1723 K that are within 0%, 5%, and 28%, respectively, of the crystalline

283   volumes of lime ($^{[6]}CaO$), periclase ($^{[6]}MgO$) and wustite ($^{[6]}FeO$) at 298 K, consistent

284   with of an average coordination for Ca^{2+}, Mg^{2+} and Fe^{2+} in these melts of ~6, ~5.8, and

285   ~4.7 (Guo et al., 2013; 2014). George and Stebbins (1998) point out that although Ni^{2+},

286   Fe^{2+} and Mg^{2+} share a similar ionic size and valence, the lower average coordination for

287   Ni^{2+} and Fe^{2+} in contrast to the higher average coordination for Mg^{2+}, may reflect a

288   difference in the bonding behavior between transition metal cations (e.g., Ni^{2+}, Fe^{2+}) and

289   alkaline earth cations (e.g., Mg^{2+}).

290   The most important conclusion to be drawn from the results in Figure 2,

291   irrespective of the cause, is that if the effect of pressure is neglected when the Mg-

292   thermometer and Ni-thermometer are both applied to a basalt that crystallized olivine at <

293   1 GPa, the expectation is that the Mg-thermometer will give a temperature that is too low,

294   whereas the Ni-thermometer will not (within 1σ uncertainty). Therefore, the value of ΔT

295   ($T_{Mg} - T_{Ni}$) is expected to be close to zero or negative, and the magnitude of ΔT will scale

296   with the depth of olivine crystallization ($\leq$ -52°C for depths $\leq$ 1 GPa).

13

297

APPLICATION TO MID-OCEAN RIDGE BASALTS

299   An opportunity to test the application of both the Mg- and Ni-thermometers

300   (Table 3, Eq. 1) on mid-ocean ridge basalt (MORB) samples is provided by the

301   petrological study of Allan et al. (1989) on a series of glassy MORB samples erupted

302   from the Lamont Seamount Chain, associated with the East Pacific Rise. Only those

303   samples from the margins of rapidly quenched pillow basalts, with a glassy groundmass

304   and sparse phenocrysts + microphenocrysts (0.4-5.4%) of olivine + plagioclase are

305   examined here (Table 5). Reported melt (glass) compositions are used to obtain

306   temperature from the Mg-thermometer (Eq.1 and Table 3), and the results range from

307   1189-1149°C.

308   The Ni contents of both the olivine phenocrysts and glass were also analyzed and

309   reported by Allan et al. (1989), enabling application of the Ni thermometer (Eq. 1 and

310   Table 3). The observed compositional range of the olivine phenocrysts within each

311   sample is narrow (~1-2% Fo) and the most Fo-rich and Ni-rich olivine composition

312   reported for each sample was used. Resulting temperatures range from 1214 to 1143°C.

313   The results of the two thermometers applied to the nine MORB samples from

314   Allan et al (1989) are summarized in Table 5, and the resulting values for ΔT (= T_{Mg}–

315   T_{Ni}) are compared to those for the 123 1-bar experimental dataset in Figure 3. The values

316   of ΔT range from +45 to -45 °C with an average of -3 ± 33˚C. The 1σ variance in the

317   calculated ΔT values for the MORB samples broadly matches that (1σ = 29°C) for the

318   123 anhydrous experiments (Fig. 3).

319

14

APPLICATION TO SUBDUCTION-ZONE BASALTS

320

321   The Ni- and Mg-thermometers from this study (Table 3, Eq. 1) were also applied

322   to a series of subduction-zone lavas that may have crystallized olivine at greater crustal

323   depths than most MORBs and contained higher melt H_2O concentrations. For this

324   application, 18 olivine-bearing lavas from the Michoacán-Guanajuato volcanic field

325   (MGVF) in the Mexican arc were chosen. The whole-rock compositions and mineral

326   modes of 16 basalt and basaltic andesite samples from a 4400 km^2 segment of the

327   MGVF, referred to as the Tancitaro-Nueva Italia region, were obtained from the study of

328   Ownby et al. (2011) and are presented in Table 6. Two additional samples from the

329   MGVF, one from Volcán Jorullo and one from Cerro La Pilita, from the study of Luhr

330   and Carmichael (1985), are also included in Table 6. Three of the 18 samples (Jor-44,

331   TAN-19 and APA-6) are from cinder cones (Volcán Jorullo, Cerro el Astillero and Cerro

332   el Hungaro, respectively) that also have been sampled by Johnson et al. (2008; 2009) in

333   their study of the volatile contents in olivine-hosted melt inclusions.

334   The 18 samples in Table 6 contain 2-10% olivine phenocrysts (defined to include

335   all crystals ≥ 300 μm), and olivine is the most abundant phenocryst in all samples. Two

336   of the samples contain a notable abundance of plagioclase phenocrysts (TAN-19 and UR-

337   2) at 4 and 5%, respectively, and they have similar compositions to NI-27 and NI-21,

338   respectively, which are free of plagioclase phenocrysts (Table 6). By including these two

339   compositional pairs of phenocryst-rich (plagioclase-bearing) and phenocryst-poor

340   (plagioclase-free) samples, any systematic difference in the thermometry results can be

341   evaluated as a function of overall phenocryst abundance.

342

343   **Application of the D_{Mg} and D_{Ni} (olivine-melt) thermometer**

344   In order to apply the $D_{Mg}^{oliv/liq}$ and $D_{Ni}^{oliv/liq}$ thermometers to a set of natural

345   samples for which no prior petrological information is available, the first task is to

346   analyze the olivine phenocrysts in each sample and evaluate whether the most Fo-rich

347   olivine in each sample could be the equilibrium composition to first crystallize from the

348   bulk liquid. A test of equilibrium is made using appropriate $^{Fe^{2+}-Mg}K_D$ (olivine-melt) values

349   from experiments in the literature. If confirmed, the most Fo-rich olivine can be used to

350   calculate temperature with the Mg-thermometer (Eq.1 and Table 3). Next, a fitted

351   relationship between Ni and Fo content in the olivines in each sample is obtained. This

352   allows an evaluation of the mean value of Ni (and its variation) in the most Fo-rich

353   olivine in each sample, which is used to calculate temperature, together with melt

354   composition, using the Ni-thermometer (Eq.1 and Table 3).

355

356   **Microprobe analyses of olivine.** Electron microprobe traverses across 20-30

357   olivine crystals were conducted in each of the 18 samples in Table 6. Traverses along the

358   long axes of each crystal were made, with an analysis every 20-30 µm, leading to

359   approximately 300-500 olivine analyses for each sample. These analyses are tabulated in

360   the supplementary material (Appendix H) and are summarized in a histogram of forsterite

361   (Fo) content for each sample (Appendix I); all samples show a continuous range of

362   olivine compositions, with no breaks. The most Fo-rich olivine composition for each

363   sample is listed in Table 6.

364

365   **A test of olivine-melt equilibrium using $^{Fe^{2+}-Mg}K_D$ values.** To evaluate whether

366   the most Mg-rich olivine in each sample represents the first olivine to crystallize from the

16

367   whole-rock melt composition, the ferric-ferrous ratio (and fO_2 condition) in the melt at

368   the onset of olivine crystallization is calculated to see if reasonable results are obtained.

369   An initial estimate for the $^{Fe^{2+}-Mg}K_D$ between olivine and melt is 0.34, which is the value

370   Matzen et al. (2011) reports on the basis of 446 anhydrous 1-bar experiments in the

371   literature, using the equation provided by Jayasuriya et al. (2004) to relate melt

372   composition, temperature and oxygen fugacity to a melt ferric-ferrous ratio. The resulting

373   Fe^{3+}/Fe^T ratios in the 18 samples in Table 6 range from 0.12 to 0.27 and correspond to

374   ΔNNO values from -1.5 to +0.8 (=$logfO_2$[sample] – $logfO_2$[Ni-NiO buffer] at the same

375   temperature from the Ni-thermometer). These Fe^{3+}/Fe^T values (average = 0.20) and

376   ΔNNO values (average = -0.1) are slightly higher relative to mid-ocean ridge basalts,

377   which is expected for subduction-zone magmas.

378   There is evidence, however, that the $^{Fe^{2+}-Mg}K_D$ between olivine and melt may be

379   affected by melt H_2O concentration, and a compilation of 108 hydrous experiments on

380   basalts, for which fO_2 is buffered or monitored, from eight studies (Sisson and Grove,

381   1993a, 1993b; Wagner et al., 1995; Righter and Carmichael, 1996; Moore and

382   Carmichael, 1998; Almeev et al., 2007; Médard and Grove, 2008; Parman et al., 2011),

383   leads to an average $K_D = 0.37 \pm 0.04$ (Appendix J), using the model equation of

384   Jayasuirya et al. (2004) to calculate melt ferric-ferrous ratios in the experimental melts.

385   When this higher $^{Fe^{2+}-Mg}K_D$ value is applied to the most Mg-rich olivine in each of the 18

386   samples in Table 6, the resulting Fe^{3+}/Fe^T ratios range from 0.19-0.32 and correspond to

387   ΔNNO values of -0.2 to +1.4. These results lead to a higher average Fe^{3+}/Fe^T ratio (0.26)

388   and a higher average ΔNNO value (+0.7) relative to those when a value of 0.34 is used,

389   and fully overlap with the range of Fe^{3+}/Fe^T values (0.19-0.28) directly analyzed in

17

390   olivine-hosted melt inclusions in arc basalts (e.g., Kelley and Cottrell, 2009; Brounce et

391   al., 2014). Therefore, there is no reason to conclude that the most Mg-rich olivine

392   composition in each sample in Table 6 is not close to the first olivine to crystallize from

393   the whole-rock liquid composition. Nonetheless, the effect of underestimating the mol%

394   Fo of the first olivine to crystallize from the melt on the thermometry results is discussed

395   below.

396

397   **Ni concentrations in olivine as a function of Fo-content.** The next step in

398   applying the Ni- thermometer (Table 3) is to determine the Ni concentration in olivine at

399   the onset of crystallization from a liquid that is represented by the whole-rock

400   composition. This can be calculated from a plot of wt% NiO as a function of mol% Fo for

401   all olivine analyses in each sample, and a linear fit to the data that span the highest 3

402   mol% Fo content for the olivine population in each sample (Fig. 4). The fitted linear

403   equation for each sample is then used to calculate the average Ni content in the most Fo-

404   rich olivine (value reported in Table 6). The minimum and maximum standard deviation

405   (1σ) in wt% NiO for the most Fo-rich olivine among the 18 samples is ±0.03 and ±0.05,

406   respectively.

407
408   **Temperatures (and uncertainties) calculated from the Mg- and Ni-**

409   **thermometers.** Application of the Mg-thermometer (Eq. 1 and Table 3), using the most

410   Fo-rich olivine analyzed in each sample together with their whole-rock composition

411   (Table 6), leads to temperatures that range from 1122 to 1240 °C for samples that range

412   from 4.3 to 9.4 wt% MgO (Table 6). For application of the Ni-thermometer (Eq. 1 and

413   Table 3), the Ni contents in olivine at the onset of crystallization were combined with the

414   Ni contents in the whole-rock samples to calculate the value of $D_{Ni}^{oliv/liq}$ at the onset of

415   olivine crystallization for each sample in Table 6. This value was then incorporated into

416   the Ni-thermometer (Eq. 1, Table 3) to calculate the temperature at which olivine first

417   began to crystallize in these 18 subduction-zone magmas. Temperatures range from 1020

418   to 1159 °C for these basalt and basaltic andesite samples (52-59 wt% SiO_2) and are

419   112°C cooler, on average, than the temperatures calculated with the updated Mg-

420   thermometer (Table 6). The uncertainties on these temperatures are estimated to be ±

421   29°C at the 1σ level, on the basis of the calibration results for ΔT on 123 experiments

422   (Table 3 and Fig. 1c). An additional uncertainty of ± 11 and ± 6 °C, respectively, is

423   added owing to an average 1σ uncertainty of ± 0.05 wt% NiO in olivine and ± 4 ppm

424   uncertainty in the average whole-rock Ni concentration.

425   Another source of error is that the first Mg-rich olivine to crystallize from the

426   melt may not be exposed on the thin-section surface and the microprobe traverse may not

427   have crossed it. It is also possible that some diffusive re-equilibration of the initial Mg-

428   rich olivine may have occurred as well. Therefore, the highest Fo content analyzed in

429   each sample may be a minimum value, and therefore the resulting temperatures derived

430   from both the Ni- and Mg-thermometer may be maximum values. The combined effect

431   on both thermometers is to cause ΔT values (=T_{Mg}-T_{Ni}) to increase by 13-46 degrees per

432   1 mol% Fo increase in olivine composition for the samples in Table 6. Therefore, the

433   reported ΔT values in Table 6 are minimum values if the most Mg-rich olivine to have

434   crystallized in each sample is not captured in the analyses.

435

436

19

437   **A comparison of ΔT (= T_{Mg}-T_{Ni}) values between hydrous basalts and MORBs**

438   The values of ΔT (= T_{Mg}– T_{Ni}) for the 18 subduction-zone samples in Table 6

439   range from 63 to 150 °C and are systematically higher than the ΔT values calculated for

440   the nine mid-ocean ridge basalts in Table 5. The comparison of these two sets of ΔT

441   values to those for the 123 experiments are illustrated in Figure 3. As discussed above,

442   neglecting the effect of pressure on the two thermometers is expected to lead to

443   underestimation of ΔT (=T_{Mg} - T_{Ni}). Therefore, the large, positive values of ΔT obtained

444   for the subduction-zone magmas in Table 6 cannot be attributed to the effect of pressure.

445   Nor can they be attributed to the effects of temperature and/or anhydrous melt

446   composition (Fig. 1c). Instead, it appears that the large positive values of ΔT reflect a

447   difference in the sensitivity of $D_{Mg}^{oliv/liq}$ and $D_{Ni}^{oliv/liq}$ to dissolved water in basaltic

448   liquids.

449

450   **A different sensitivity of $D_{Mg}^{oliv/liq}$ and $D_{Ni}^{oliv/liq}$ to dissolved water in the melt?**

451   As noted in the introduction, all thermometers based on $D_{Mg}^{oliv/liq}$ (e.g., Beattie,

452   1993) require a major correction for dissolved H_2O in the melt, possibly because

453   hydroxyl groups complex with Mg^{2+} to lower the activity of the MgO component in

454   hydrous melts (e.g, Waters and Lange, 2013). The strong dependence of Mg-

455   thermometers on melt H_2O concentration was reviewed by Putrika et al. (2007), and the

456   effect is illustrated in Figure 5 using the experimental datasets of Almeev et al. (2007)

457   and Médard and Grove (2008) at ≤ 200 MPa. In these two studies, detailed experimental

458   approaches were applied to precisely locate the depression of the olivine liquidus with

459   increasing melt H_2O concentration. Application of the updated Mg-thermometer (Table

20

460   3, Eq.1) gives the anhydrous temperature for each experiment, whereas the Putirka et al.

461   (2007) thermometer (with an H_2O correction, Table 4) gives the hydrous temperature.

462   The differences between the two thermometers lead to ΔT values $(=T_{anhydrous}-T_{hydrous})$ that

463   are consistently positive and increase with the amount of dissolved water in the

464   experimental melt (Fig. 5). This result illustrates that $D_{Mg}^{oliv/liq}$ has a strong sensitivity to

465   dissolved water in basaltic melts, and it suggests that the reason why the Ni-thermometer

466   gives lower temperatures than the Mg-thermometer when applied to hydrous samples

467   (Table 6, Fig. 3) is because $D_{Ni}^{oliv/liq}$ is less sensitive to water. The question that arises is

468   whether the Ni-thermometer (Table 3, Eq. 1), which has no H_2O correction, gives similar

469   temperatures as the Mg-thermometer of Putirka et al. (2007), which has an H_2O

470   correction.

471   This question is addressed with three of the 18 samples in Table 6 (Jor-44, TAN-

472   19 and APA-6), for which melt H_2O concentrations were directly analyzed in olivine-

473   hosted melt inclusions (Johnson et al., 2008; 2009). The maximum H_2O concentrations

474   reported for these three samples (5.7, 4.6 and 3.9 wt%, respectively) can be used in the

475   Mg-thermometer of Putirka et al. (2007; their Eq. 4), which incorporates the

476   compositional effect of melt H_2O, to obtain the temperature of these magmas at the onset

477   of olivine crystallization. The results are 1139, 1116 and 1099°C, respectively, for the

478   Jor-44, TAN-19 and APA-6 melts with 5.7, 4.6 and 3.9 wt% H_2O, respectively, at

479   minimum entrapment pressures of 0.4, 0.15 and 0.1 GPa (Johnson et al., 2008; 2009).

480   These temperatures are within -38, +38 and +24°C, respectively, of the temperatures

481   obtained in this study using the Ni-thermometer (Table 3, Eq. 1). These differences are

482   well within the combined 1σ uncertainty of the two thermometers ($\pm$ 29 °C for Ni-

21

483   thermometer, Table 3, Eq. 1; ± 31°C for Putirka et al., 2007; Table 4). This result

484   supports the inference that D_{Ni} is less sensitive than D_{Mg} to dissolved water in the melt,

485   which can be further tested with a set of hydrous olivine-melt equilibrium experiments.

486
487   **Ni-partitioning results on hydrous olivine-melt experiments.** Although

488   Almeev et al. (2007) and Médard and Grove (2008) did not report Ni concentrations in

489   olivine and melt, a preliminary evaluation of how melt H_2O content affects the Ni-based

490   thermometer is made in this study through new Ni-partitioning results on the run products

491   from a hydrous phase-equilibrium study on a basaltic andesite (MAS-22; Moore and

492   Carmichael, 1998). In that study, there were three experimental run products that contain

493   glass + olivine only (runs 22-2, 22-7 and 22-12), with olivine abundance reported to be

494   ≤3% (run conditions are summarized in Table 7). The olivine crystals and quenched

495   liquid (glass) from these three experiments were analyzed in this study for their Ni

496   contents. The results are tabulated in Table 7.

497   These values of $D_{Ni}^{oliv/liq}$ were calculated from the newly obtained Ni data from

498   the three experimental charges, and were used to calculate the amount of olivine that

499   crystallized during each of these phase-equilibrium runs, as a check on internal

500   consistency, using the equilibrium crystallization equation:

$$\frac{C_L}{C_O} = \frac{1}{D_{Ni}^{ol/melt}(1-F)+F}$$ (5)

502   In Equation 5, C_L is the analyzed concentration of Ni in the quenched liquid phase, C_O is

503   the initial concentration of Ni in the liquid prior to olivine crystallization (106 ppm in the

504   MAS-22 whole rock; Lange and Carmichael, 1990) and F is the melt fraction. On the

505   basis of this equation and the $D_{Ni}^{oliv/liq}$ values for each experiment, the abundance of

22

506   olivine ranges from 1.4 to 3.6%, which is consistent with the values reported by Moore

507   and Carmichael (1998).

508   Using the compositional data reported in Table 7, the calculated Ni-temperatures

509   (Table 3, Eq.1) for the three experiments lead to residuals (T_{Ni} -T_{expt}) of +24, -50, and -

510   21 °C for melt H_2O contents of 2.5, 3.2 and 5.0 wt%, respectively (Table 7). When these

511   residuals are plotted in Figure 1a, they are well within the range of the residuals for the

512   123 1-bar experiments upon which the Ni-thermometer (Table 3, Eq. 1) is calibrated on.

513   This result strongly suggests that the Ni-based olivine-melt thermometer has a relatively

514   weak dependence on melt H_2O contents.

515   Understanding the underlying cause for why $D_{Ni}^{oliv/liq}$ appears to have a lower

516   sensitivity than $D_{Mg}^{oliv/liq}$ to dissolved water in the melt is of key importance. However, it

517   is beyond the scope of the present study to answer this question because it requires a

518   spectroscopic study of the coordination environments for both Ni and Mg in the same

519   basaltic melts under hydrous conditions, which are not yet available. Nonetheless,

520   available spectroscopic evidence (e.g., Galoisy and Calas, 1993; George and Stebbins,

521   1998), supported by liquid density measurements (Guo et al., 2013; 2014), show that

522   alkaline earth cations, such as Mg^{2+}, and transition metal cations, such as Fe^{2+} and Ni^{2+},

523   display different bonding behavior despite their similar size, and these differences may

524   extend to hydrous melts. As an aside, it may that the partition coefficients for Mn^{2+} and

525   Co^{2+}, two other transition metals with an ionic radius similar to that for Ni^{2+}, may also

526   lead to useful olivine-melt thermometers that are weakly dependent on water in the melt

527   phase. In the meantime, the accuracy of the Ni-thermometer, which does not include an

23

528   H_2O correction, can be evaluated through a comparison of its results to experimentally

529   determined hydrous phase diagrams.

530

531   **Consistency with hydrous phase-equilibrium experiments on basaltic andesite**

532   The results from the Ni-thermometer (Table 3, Eq.1) for APA-6 (Table 6) can be

533   compared to the hydrous phase-equilibrium experimental results from Moore and

534   Carmichael (1998) on the MAS-22 basaltic andesite (Table 7), which has a similar

535   composition to APA-6. In Figure 6, a simplified plot of the phase stability fields for

536   olivine, plagioclase, and hornblende are shown on a plot of P_{H2O} vs. temperature based on

537   the results of Moore and Carmichael (1998). Also shown are isopleths of melt H_2O

538   concentration based on the H_2O solubility model of Zhang et al. (2007). The calculated

539   temperature for APA-6 at the onset of olivine crystallization is 1075 ($\pm$ 29) °C, which is

540   projected onto the phase diagram in Figure 6 (the phase diagram of MAS-22 with all

541   individual experiments plotted is shown in Appendix K).

542   The occurrence of large, sparse phenocrysts of olivine in APA-6 with diffusion-

543   limited (i.e., rapid-growth) textures (Fig. 7) indicates that this basaltic andesite liquid

544   experienced significant effective undercooling ($\Delta T_{eff} = T_{liquidus} - T_{melt}$) during phenocryst

545   growth (e.g., Lofgren, 1974; Welsch et al., 2014). It is difficult for a melt to develop an

546   undercooling during slow cooling and crystallization in a magma chamber. In contrast, an

547   effective undercooling during phenocryst growth readily develops during rapid ascent

548   under fluid-saturated conditions, owing to the effect of H_2O degassing from the melt

549   (e.g., Waters et al., 2015). A projected ascent path for APA-6 under fluid-saturated

550   conditions is illustrated in Figure 6, and it is consistent with the P_{H2O}-T location for the

24

551   entrapment of the olivine-hosted melt inclusion with 3.9 wt% H_2O from Johnson et al.

552   (2008).

553   The results for two additional samples (UR-2 and NI-21) can also be projected

554   onto this experimental phase diagram, as their compositions only differ from MAS-22

555   (Table 7) and APA-6 by having slightly lower MgO concentrations (Table 6). The

556   results for UR-2 and NI-21 are particularly noteworthy, as the samples have nearly

557   identical bulk compositions (despite being erupted from separate vents located tens of km

558   apart; Ownby et al., 2011) and give similar temperatures (1020 and 1021 °C) at the onset

559   of olivine crystallization, suggestive of similar melt H_2O contents. However, they

560   contain very different phenocryst abundances. UR-2 contains ~5% olivine and ~5%

561   plagioclase, whereas NI-21 only contains ~4% olivine with diffusion-limited (i.e., rapid

562   growth) textures (Fig. 7). The absence of plagioclase phenocrysts could reflect a kinetic

563   delay to its nucleation and growth in NI-21 during its fluid-saturated ascent, similar to

564   what has been documented for various phenocryst-poor andesite, dacite and rhyolite

565   melts (e.g., Frey and Lange, 2011; Crabtree and Lange, 2011; Waters and Lange, 2013;

566   Waters et al., 2015). The inference, therefore, is that NI-21 ascended more rapidly than

567   UR-2 to the surface. A similar difference in ascent rate and timescale for phenocryst

568   growth may explain the difference in phenocryst abundance between TAN-19 and NI-27,

569   which have similar bulk compositions (Table 6). The absence of plagioclase phenocrysts

570   in NI-27, together with the abundance of olivine phenocrysts with diffusion-limited

571   growth textures (Fig. 7), is consistent with a kinetic delay to plagioclase nucleation and

572   growth during rapid ascent under fluid-saturated conditions (e.g., Waters et al., 2015).

573

574 **Consistency with phase-equilibrium experiments on hornblende-bearing basalt**

575   Another comparison of thermometry results with hydrous phase-equilibrium

576   experiments can be made for lava flow sample Jor-46d, which is the only sample among

577   the 18 samples in Table 6 to have hornblende in its phenocryst assemblage. In Figure 8, a

578   simplified plot of the phase stability fields for olivine, clinopyroxene, and hornblende are

579   shown on a plot of P_{H2O} vs. temperature based on the experimental results of Barclay and

580   Carmichael (2004) on Jor-46, a scoria sample from the same cinder cone as the lava flow

581   sample Jor-46d; Luhr and Carmichael, 1985. The phase diagram of Jor-46 with all

582   individual experiments plotted is shown in Appendix K. The extrapolated dT/dP_{H2O} slope

583   of the hornblende-in curve in Figure 8 between P_{H2O} = 200 and 500 MPa is estimated

584   from the experimentally established hornblende-in curve over this P_{H2O} interval by

585   Krawczynski et al. (2012) for a high-Mg andesite. Also shown in this phase diagram is

586   the calculated temperature (1105 ± 29 °C; gray shaded rectangle) at the onset of olivine

587   crystallization from the Ni-thermometer (Table 3, Eq. 1). Within the 1σ uncertainty of

588   the Ni-thermometer, the onset of olivine crystallization and the stability field of

589   hornblende overlap, which shows that it is plausible that the phenocryst assemblage in

590   Jor-46d crystallized during fluid-saturated ascent, with undercooling driven by degassing

591   of dissolved H_2O. An alternative model is that the phenocryst assemblage grew during

592   cooling at $P_{H2O} \geq$ 200 MPa. Either way, the results of the Ni-thermometer are consistent

593   with the observed phenocryst assemblage and the phase-equilibrium results of Barclay

594   and Carmichael (2004) and indicate that the onset of phenocryst crystallization in Jor-46d

595   occurred at melt H_2O contents $\geq$ 5.5 wt% H_2O, and possibly higher (>7 wt% H_2O; Fig.

596   8).

26

597

MINIMUM MELT WATER CONTENTS

Relationship between ΔT and dissolved H_2O in the melt

There is an opportunity to use the difference in calculated temperatures from the

Mg- and Ni-thermometers, when applied to hydrous samples, as a proxy for an estimate

of $\Delta T = T_{anhydrous}-T_{hydrous}$.   This, in turn, allows broad constraints to be placed on the

minimum melt H_2O concentrations in hydrous magmas at the onset of olivine

crystallization. As discussed above, Almeev et al. (2007) and Médard and Grove (2008)

conducted experiments to carefully quantify the depression of the olivine liquidus

temperature ($\Delta T = T_{anhydrous}-T_{hydrous}$) as a function of melt H_2O concentration. In Figure

9, their experimental results are plotted together with several additional hydrous olivine-

melt equilibrium experiments from the literature (Sisson and Grove, 1993a and 1993b;

Parman et al., 2011; Wagner et al., 1995; Berndt et al., 2005; Moore and Carmichael

1998) under near-liquidus conditions ($\leq 5\%$ olivine). Note that there is a wide range of

ΔT values for melt H_2O concentrations of ~5 wt% recorded by these experiments (Fig. 9).

Detailed information for these 36 olivine-melt equilibrium experiments are reported in

Appendix L. For the purposes of internal consistency, the anhydrous liquidus

temperature ($T_{anhydrous}$) for each experiment was calculated with the Mg- thermometer

(Table 3 and Eq.1) and the pressure correction of Herzberg and O'Hara (2002) as shown

in Eq. 2. The experimental temperature is treated as a close approximation to the hydrous

liquidus temperature ($T_{hydrous}$) for each experiment. The melt H_2O concentration for all

pure-H_2O fluid-saturated experiments was calculated using the Zhang et al. (2007) water

solubility model ($1\sigma = \pm0.34$ wt%). For the water under-saturated experiments of

620   Almeev et al. (2007), the H_2O contents measured by Karl Fischer Titration (KFT) were

621   used, and when unavailable, the H_2O contents measured by FTIR (Fourier transform

622   infrared) spectroscopy were used. Phase-equilibrium experiments at $P_{H2O} \geq 500$ MPa

623   were not included in this compilation (e.g., Hamilton, 1964) because the calculated water

624   concentrations in those melts have a relatively high uncertainty (Zhang et al., 2007).

625   The goal in this study is to provide a simple polynomial equation that describes

626   the lower limit of the data in Figure 9 and allows a minimum melt H_2O content to be

627   calculated from values of ΔT ($= T_{anhydrous} - T_{hydrous} = T_{Mg} - T_{Ni}$). The second order

628   polynomial curve fit to data points with the lowest melt H_2O content for their ΔT is:

629                    $$\text{wt\% } H_2O = 6.92 \times 10^{-5} \times \Delta T^2 - 2.62 \times 10^{-2} \times \Delta T \qquad (6)$$

630   The application of Equation 6 to the average ΔT result (-3°C) for the nine MORBs in

631   Table 5 leads to a melt H_2O content of 0 wt%, which is consistent with previous work

632   that documents relatively low melt H_2O contents in mid-ocean ridge basalts (e.g.,

633   Danyushevsky, 2001). The application of Equation 6 to the average ΔT result (112°C)

634   for the 18 subduction-zone magmas in Table 6 leads to an average minimum H_2O melt

635   content of 3.8 wt%. This result is consistent with direct measurements of H_2O

636   concentrations in olivine-hosted melt inclusions in arc basalts (e.g., Sisson and Layne,

637   1993; Cervantes and Wallace, 2003; Walker et al., 2003; Wade et al., 2006; Benjamin et

638   al., 2007; Portnyagin et al., 2007; Sadofsky et al., 2008; Shaw et al., 2008; Johnson et al.,

639   2009; Kelley et al., 2010; Zimmer et al, 2010; Ruscitto et al., 2010, 2011, Lloyd et al.,

640   2013), which show that they contain up to 7 wt% H_2O, with an average that is close to ~4

641   wt% H_2O (Plank et al., 2013).

642

28

643 **Application of plagioclase-liquid hygrometry to two olivine-bearing andesites**

644   There may be an opportunity to extend the plagioclase-liquid hygrometer, which

645 requires an independent assessment of temperature, to olivine-bearing andesites when

646 used in conjunction with the Ni-thermometer (Table 3, Eq.1). Many phenocryst-poor

647 low-SiO_2 andesites do not contain ilmenite, and therefore temperatures cannot be

648 obtained from two Fe-Ti oxides (e.g. Ghiorso and Evans, 2008). Two of the 18 samples

649 in Table 6 are olivine-bearing andesites with 59 wt% SiO_2 and 4.3 wt% MgO (UR-60 and

650 UR-61). In comparison to the phase relations for the basaltic andesite MAS-22 (Fig. 6),

651 which has 55.5 wt% SiO_2 and 6.5 wt% MgO, it is probable that the positions of the

652 plagioclase-in and olivine-in curves for these two andesites are relatively close in P_{H2O}-T

653 space.

654   In order to apply the plagioclase-liquid hygrometer, the compositions of the

655 plagioclase phenocrysts in the two samples were analyzed in this study. The microprobe

656 results are given in the supplementary materials (Appendix M). The most calcic

657 plagioclase crystals in UR-60 and UR-61 are An_{83} and An_{82}, respectively, which results

658 in calculated melt water contents of ~2.9 and ~2.5 wt%, respectively, at the onset of

659 plagioclase crystallization in each sample, at temperatures of 1046 and 1050 °C,

660 respectively. In this case, an uncertainty ± 29°C in temperature propagates to an

661 uncertainty in melt H_2O of ± 0.4 wt% from the plagioclase hygrometer, and the results

662 are consistent with the minimum estimates of melt H_2O content for these two samples

663 using Equation 6 (Table 6; 2.6 and 2.2 wt%, respectively).

664

665   **IMPLICATIONS**

29

666   Currently, all olivine-melt thermometers that are based on $D_{Mg}^{oliv/liq}$ need a

667   correction for the H_2O content in the melt, which in turn requires that it be measured.

668   Unfortunately, the process of obtaining high-quality H_2O analyses from olivine-hosted

669   melt inclusions is labor and time intensive, at least compared to microprobe analyses of

670   olivine. Moreover, magmas that erupt explosively (i.e., scoria) vs. effusively (i.e., lavas)

671   are more likely to contain olivine-hosted melt inclusions that preserve maximum pre-

672   eruptive H_2O contents, but they are generally less well preserved in the field (e.g., Lloyd

673   et al., 2012). Therefore, in order to compile large global data sets on the temperatures of

674   hydrous basalts, it is desirable to develop an olivine-melt thermometer that only requires

675   microprobe analyses to apply and has a negligible dependence on water.

676   In some arcs, it has been shown that the amount of dissolved H_2O in erupted

677   basalts decreases with increasing distance from the trench, which is inferred to reflect a

678   shift from H_2O-induced flux melting beneath the volcanic front to decompressional

679   melting in the back arc (Walker et al., 2003, Johnson et al, 2009).   An olivine-melt

680   thermometer that has a small dependence on dissolved H_2O in the melt allows a test of

681   whether there is a corresponding systematic change in the temperature of basaltic melts

682   with distance from the trench, which will enhance our understanding of the interplay

683   between flux melting and decompressional melting at subduction zones. The Ni-

684   thermometer in this study (Table 3, Eq. 1) requires relatively routine whole rock analyses

685   combined with microprobe analyses on olivine, and thus it can be used to generate

686   relatively large datasets to examine temperature variations in mantle-derived arc basalts

687   on a global basis.

688   Application of the Ni-thermometer can also be made to olivine-bearing lavas

689   associated with plumes, including Yellowstone and Iceland, for which there is evidence

690   of dissolved H_2O contents up to 3.3 and 1.0 wt% H_2O, respectively, (e.g., Stefano et al.

691   2011; Nichols et al., 2002), and therefore a thermometer is needed that does not require

692   prior information on water concentrations in the melt. It may also be possible to apply the

693   Ni-thermometer to Archean komatiites, for which there is ongoing debate about whether

694   they erupted at very high temperatures (>1500 °C) (e.g., Herzberg et al., 2007; Sobolev et

695   al., 2016), or whether they erupted at significantly lower temperatures owing to relatively

696   high melt H_2O concentrations (e.g., Grove and Parman, 2004; Parman et al., 2004). The

697   results from this study suggest that an olivine-melt thermometer based on D_{Ni} has

698   considerable promise to help resolve this controversy, after additional Ni-partitioning

699   olivine-melt equilibrium experiments are obtained under hydrous conditions.

700

701   **ACKNOWLEDGEMENT**

706

707   **REFERENCES**

708   Agee, C. B., and Walker, D. (1990) Aluminum partitioning between olivine and

709   ultrabasic silicate liquid to 6 GPa. Contributions to Mineralogy and Petrology, 105, 243-

710   254.

711   Allan, J.F., Batiza, R., Perfit, M.R., Fornari, D.J., Sack, R.O. (1989) Petrology of lavas

712   from the Lamont Seamount Chain and adjacent East Pacific Rise, 10˚N. Journal of

713   Petrology, 30, 1245-1298.

714   Almeev, R.A., Holtz, F., Koepke, J., Parat, F., Botcharnikov, R.E. (2007) The effect of

715   H_2O on olivine crystallization in MORB: experimental calibration at 200 MPa. American

716   Mineralogist, 92, 670-674.

717   Arndt, N.T. (1977) Partitioning of nickel between olivine and ultrabasic and basic

718   komatiite liquids. Carnegie Institution of Washington Yearbook, 76, 553-557.

719   Asimow, P.D., Hirschmann, M.M., Stolper, E.M. (2001). Calculation of peridotite partial

720   melting from thermodynamic models of minerals and melts, IV. Adiabatic decompression

721   and the composition and mean properties of mid-ocean ridge basalts. Journal of

722   Petrology, 42, 963-998.

723   Barclay, J., and Carmichael, I.S.E. (2004) A hornblende basalt from western Mexico:

724   water-saturated phase relations constrain a pressure-temperature window of eruptibility.

725   Journal of Petrology, 45, 485-506.

726   Beattie, P., Ford, C., Russell, D. (1991) Partition coefficients for olivine-melt and

727   orthopyroxene-melt systems. Contributions to Mineralogy and Petrology, 109, 212-224.

728   Beattie, P. (1993) Olivine-melt and orthopyroxene-melt equilibria. Contributions to

729   Mineralogy and Petrology, 115, 103-111.

730   Benjamin, E.R., Plank, T., Wade, J.A., Kelley, K.A., Hauri, E.H., Alvarado, G.E. (2007)

731   High water contents in basaltic magmas from Irazu Volcano, Costa Rica. Journal of

732   Volcanology and Geothermal Research, 168, 68-92.

733   Berndt, J., Koepke, J., Holtz, F. (2005) An experimental investigation of the influence of

734   water and oxygen fugacity on differentiation of MORB at 200 MPa. Journal of Petrology,

735   46, 135-167.

736   Bird, M.L. (1971) Distribution of trace elements in olivine and pyroxenes – An

737   experimental study. Ph.D. Thesis, University of Missouri, Rolla.

738   Brounce, M.N., Kelley, K.A., Cottrell E. (2014) Variations in $Fe^{3+}/\Sigma Fe$ of Mariana Arc

739   basalts and mantle wedge fO_2. Journal of Petrology, 55, 2513-2536.

740   Cervantes, P., and Wallace, P.H. (2003) Role of H_2O in subduction-zone magmatism:

741   new insights from melt inclusions in high-Mg basalts from central Mexico. Geology, 31,

742   235-238.

743   Crabtree, S.M., and Lange, R.A. (2011) Complex phenocryst textures and zoning patterns

744   in andesites and dacites: evidence of degassing induced rapid crystallization? Journal of

745   Petrology, 52, 3–38.

746   Danyushevsky, L.V. (2001) The effect of small amounts of H_2O crystallisation of mid-

747   ocean ridge and backarc basin magmas. Journal of Volcanology and Geothermal

748   Research, 110, 265-280.

749   Ehlers, K., Grove, T.L., Sisson, T.W., Recca, S.I., Zervas, D.A. (1992) The effect of

750   oxygen fugacity on the partitioning of nickel and cobalt between olivine, silicate melt,

751   and metal. Geochimica et Cosmochimica Acta, 56, 3733–3743.

752   Falloon, T.J., Danyushevsky, L.V., Ariskin, A., Green, D.H., Ford, C.E. (2007) The

753   application of olivine geothermometry to infer crystallization temperature of parental

33

754   liquids: Implications for the temperature of MORB magmas. Chemical Geology, 241,

755   207-233.

756   Frey, H.M., and Lange, R.A. (2011) Phenocryst complexity in andesites and dacites from

757   the Tequila volcanic field, Mexico: resolving the effects of degassing vs. magma mixing.

758   Contributions to Mineralogy and Petrology, 162, 415–445.

759   Ford, C. E., D. G. Russell, J. A. Craven, and M. R. Fisk (1983), Olivine-liquid equilibria:

760   Temperature, pressure and composition dependence of the crystal/liquid cation partition

761   coefficients for Mg, Fe^{2+}, Ca and Mn. Journal of Petrology, 24, 256–265.

762   Gaetani, G.A., and Grove, T.L. (1997) Partitioning of moderately siderophile elements

763   among olivine, silicate melt, and sulfide melt: constraints on core formation in the Earth

764   and Mars. Geochimica et Cosmochimica Acta, 61, 1829-1846.

765   Galoisy, L., and Calas G. (1993) Structural environment of nickel in silicate glass/melt

766   system: Part 1. Spectroscopic determination of coordination states. Geochimica et

767   Cosmochimica Acta, 57, 3613-3626.

768   George, A.M., and Stebbins, J.F. (1998) Structure and dynamics of magnesium in silicate

769   melts: A high-temperature ^{25}Mg NMR study. American Mineralogist, 83, 1022-1029.

770   Genske, F.S., Turner, S.P., Beier, C., Schaefer, B.F. (2012) The petrology and

771   geochemistry of lavas from the Western Asores Islands of Flores and Corvo. Journal of

772   Petrology, 53, 1673-1708.

773   Ghiorso, M.S., and Sack, R.O. (1995) Chemical mass-transfer in magmatic processes IV.

774   A revised and internally consistent thermodynamic model for the interpolation and

775   extrapotion of liquid-solid equilibria in magmatic systems at elevated temperatures and

776   pressures. Contributions to Mineralogy and Petrology, 119, 197-212.

777   Ghiorso, M.S., and Evans, B.W. (2008) Thermodynamics of rhombohedral oxide solid

778   solutions and a revision of the Fe-Ti two oxides geothermometers and oxygen-barometer.

779   Americal Journal of Science, 308, 957-1039.

780   Grove, T. L., and Parman, S.W. (2004) Thermal evolution of the Earth as recorded by

781   komatiites. Earth and Planetary Science Letters, 219, 173-187.

782   Guo, X., Lange, R.A., Ai, Y. (2013) The density and compressibility of $CaO-FeO-SiO_2$

783   liquids at one bar: Evidence for four-coordinated Fe^{2+} in the $CaFeO_2$ component.

784   Geochimica et Cosmochimica Acta, 120, 206-219.

785   Guo, X., Lange, R.A., Ai, Y. (2014) Density and sound speed measurements on model

786   basalt (An-Di-Hd) liquids at one bar: New constraints on the partial molar volume and

787   compressibility of the FeO component. Geochimica et Cosmochimica Acta, 388, 283-

788   292.

789   Hamilton, D.L., Burnham, C.W., Osbom, E.F. (1964) The solubility of water and effects

790   of oxygen fugacity and water content on crystallization in mafic magmas. Journal of

791   Petrology, 5, 21-39.

792   Hart, S.R., and Davis, K.E. (1978) Nickel partitioning between olivine and silicate melt.

793   Earth and Planetary Science Letters, 40, 203–219.

794   Herzberg, C., and O'Hara, M.J. (2002) Plume-associated ultramafic magmas off

795   Phanerozoic age. Journal of Petrology, 43, 1857-1883.

796   Herzberg, C., Asimow, P.D., Arndt, N., Niu, Y., Lesher, C.M., Fitton, J.G., Cheadle,

797   M.J., Saunders, A.D. (2007) Temperatures in ambient mantle and plumes: constraints

798   from basalts, picrites, and komatiites. Geochmistry, Geophysics, Geosystems, 8, Q02006.

799   Herzberg, C., and Gazel, E. (2009) Petrological evidence for secular cooling in mantle

800   plumes. Nature, 458, 619-623.

801   Herzberg, C., and Asimow, P.D. (2015) PRIMELT3 MEGA.XLSM software for primary

802   magma calculation: peridotite primary magma MgO contents from the liquidus to the

803   solidus. Geochemistry, Geophysics, Geosystems, 16, 563-578.

804   Hirschmann, M.M., Ghiorso, M.S., Davis, F.A., Gordon, S.M., Mukherjee, S., Grove,

805   T.L., Krawczynski, M., Médard, E., Till, C.B. (2008) Library of Experimental Phase

806   Relations (LEPR): a database and web portal for experimental magmatic phase equilibria

807   data. Geochemistry, Geophysics, Geosystems, 9, Q03011.

808   Jayasuriya, K. D., O'Neill, H. St. C., Berry, A. J., Campbell, S. J. (2004) A Mössbauer

809   study of the oxidation state of Fe in silicate melts. American Mineralogist, 89, 1597-

810   1609.

811   Johnson, E.R., Wallace, P.J., Cashman, K.V., Delgado-Granados, H., Kent, A.J.R. (2008)

812   Magmatic volatile contents and degassing-induced crystallization at Volcán Jorullo,

813   Mexico: Implications for melt evolution and the plumbing systems of monogenetic

814   volcanoes. Earth and Planetary Science Letters, 269, 478-487.

815   Johnson, E.R., Wallace, P.J., Granados, H.D., Manea, V.C., Kent, A.J.R., Bindeman,

816   I.N., Donegan, C.S. (2009) Subduction-related volatile recycling and magma generation

36

817   beneath Central Mexico: Insights from melt inclusions, oxygen isotopes and geodynamic

818   models. Journal of Petrology, 50, 1729-1764.

819   Jones, J., O'Neill, H.S., Berry, A. (2011) Differential changes in Ni^{2+}, Co^{2+} and Fe^{2+}

820   coordination in silicate melt with pressure. Goldschmidt Conference Abstract,

821   Mineralogical Magazine, 75, 1124.

822   Jurewicz, A.J.G., Mittlefehldt, D.W., Jones, J.H. (1993) Experimental partial melting of

823   the Allende (CV) and Murchison (CM) chondrites and the origin of asteroidal basalts.

824   Geochimica et Cosmochimica Acta, 57, 2123-2139.

825   Kelemen, P.B., Hart, S.R., Bernstein, S. (1998) Silica enrichment in the continental upper

826   mantle via melt/rock reaction. Earth and Planetary Science Letters, 164, 387–406.

827   Kelley, K.A., and Cottrell E. (2009) Water and the oxidation state of subduction zone

828   magmas. Science, 325, 605-607.

829   Kelley, K.A., Plank, T., Newman, S., Stolper, E., Grove, T.L., Parman, S., Hauri, E.

830   (2010) Mantle melting as a function of water content beneath the Mariana arc. Journal of

831   Petrology, 51, 1711-1738.

832   Kent, A.J.R., Stolper, E.M., Francis, D., Woodhead, J., Frei, R., Eiler, J. (2004) Mantle

833   heterogeneity during the formation of the North Atlantic Igneous Province: Constraints

834   from trace element and Sr-Ni-Os-O isotope systematics of Baffin Island picrites.

835   Geochemistry Geophysics Geosystems, 5, Q11004.

836   Kinzler, R.J., Grove, T.L., Recca, S.I. (1990) An experimental study on the effect of

837   temperature and melt composition on the partitioning of nickel between olivine and

838   silicate melt. Geochimica et Cosmochimica Acta, 54, 1255–1265.

839   Krawczynski, M.J., Grove, T.L., Behrens, H. (2012) Amphibole stability in primitive arc

840   magmas: effects of temperature, H_2O content and oxygen fugacity. Contributions to

841   Mineralogy and Petrology, 164, 317-339

842   Lange, R.A., and Carmichael, I.S.E. (1990) Hydrous basaltic andesites associated with

843   minette and related lavas in Western Mexico. Journal of Petrology, 31, 1225-1259.

844   Lee, C.T., Luffi, P., Plank, T., Dalton, H., Leeman, W.P. (2009) Constraints on the depths

845   and temperatures of basaltic magma generation on Earth and other terrestrial planets

846   using new thermobarometers for mafic magmas. Earth and Planetary Science Letters,

847   279, 20-33.

848   Leeman, W.P., and Lindstrom, D.J. (1978). Partitioning of Ni^{2+} between basaltic and

849   synthetic melts and olivines: an experimental study. Geochimica et Cosmochimica Acta,

850   42, 801–806.

851   Li, C., and Ripley, E.M. (2010) The relative effects of composition and temperature on

852   olivine-liquid Ni partitioning: statistical deconvolution and implications for petrologic

853   modeling. Chemical Geology, 275, 99–104.

854   Lloyd, A.S., Plank, T., Ruprecht, P., Hauri, E., Rose, W. (2013) Volatile loss from melt

855   inclusions in pyroclasts of differing sizes. Contributions to Mineralogy and Petrology,

856   165, 129-153.

857   Lofgren, G. (1974) An experimental study of plagioclase crystal morphology: isothermal

858   crystallization. American Journal of Science, 274, 243-273.

859   Luhr, J.F., and Carmichael, I.S.E. (1985) Jorullo Volcano, Michoacán, Mexico (1759-

860   1774): The earliest stages of fractionation in calc-alkaline magmas. Contributions to

861   Mineralogy and Petrology, 90, 142-161.

862   Matzen, A. K., Baker, M. B., Beckett, J. R., Stolper, E. M. (2011) Fe-Mg partitioning

863   between olivine and high-magnesian melts and the nature of Hawaiian parental liquids.

864   Journal of Petrology, 52,1243-1263.

865   Matzen, A.K., Baker, M.B., Beckett, J.R., Stolper, E.M. (2013) The temperature and

866   pressure dependence of nickel partitioning between olivine and silicate melt. Journal of

867   Petrology, 54, 2521-2545.

868   Médard, E., and Grove, T.L. (2008) The effect of H_2O on the olivine liquidus of basaltic

869   melts: experiments and thermodynamic models. Contributions to Mineralogy and

870   Petrology, 155, 417-432.

871   Moore, G., and Carmichael, I.S.E. (1998) The hydrous phase equilibria (to 3 kbar) of an

872   andesite and basaltic andesite from western Mexico: constraints on water content and

873   conditions of phenocryst growth. Contributions to Mineralogy and Petrology, 130:304-

874   319.

875   Mysen, B.O., Virgo, D., Seifert, F.A. (1985) Relationships between properties and

876   structure of aluminosilicate melts. American Mineralogist, 70, 88-105.

877   Mysen, B.O. (2006) Redox equilibria of Iron and silicate melt structure: Implications for

878   olivine/melt element partitioning. Geochimica et Cosmochimica Acta, 70, 3121-3138.

879 Mysen, B.O. (2007a) Olivine/melt transition metal partitioning, melt composition, and

880 melt structure—influence of Al^{3+} for Si^{4+} substitution in the tetrahedral network of

881 silicate melts. Geochimica et Cosmochimica Acta, 71, 5500–5513.

882 Mysen, B.O. (2007b) Partitioning of calcium, magnesium, and transition metals between

883 olivine and melt governed by the structure of the silicate melt at ambient pressure.

884 American Mineralogist, 92, 844–862.

885 Mysen, B.O. (2008) Olivine/melt transition metal partitioning, melt composition, and

886 melt structure — melt polymerization and Q^n-speciation in alkaline earth silicate systems.

887 Geochimica et Cosmochimica Acta, 72, 4796–4812.

888 Nabelek, P.I. (1980) Nickel partitioning between olivine and liquid in natural basalts:

889 Henry's Law behavior. Earth and Planetary Science Letters, 48, 293–302.

890 Neave, D.A., Maclennan, J., Thordarson, T., Hartley, M.E. (2015) The evolution and

891 storage of primitive melts in the Eastern Volcanic Zone of Iceland: the 10ka Grímstötn

892 tephra series (i.e. the Saksunarvatn ash). Contributions to Mineralogy and Petrology, 170,

893 21.

894 Nichols, A.R.L., Carroll, M.R., Höskuldsson, Á. (2002) Is the Iceland hot spot also wet?

895 Evidence from the water contents of undegassed submarine and subglacial pillow basalts.

896 Earth and Planetary Science Letters, 202, 77-87.

897 Ownby, S.E., Lange, R.A., Hall, C.M., Delgado-Granados, H. (2011) Origin of andesite

898 in the deep crust and eruption rates in the Tancítaro-Nueva Italia region of the central

899 Mexican arc. Geological Society of America Bulletin, 123, 274-294.

900   Parman, S.W., Dann, J.C., Grove, T.L., de Wit, M.J. (1997) Emplacement conditions of

901   komatiite magmas from the 3.49Ga Komati Formation, Barberton Greenstone Belt, South

902   Africa. Earth and Planetary Science Letters, 150, 303-323.

903   Parman, S.W., Grove, T.L., Dann, J.C. (2004) A subduction origin for komatiites and

904   cratonic lithospheric mantle. South African Journal of Geology, 107, 107-118.

905   Parman, S.W., Grove, T.L., Kelley, K.A., Plank, T. (2011) Along-arc variations in the

906   pre-eruptive H_2O contents of Mariana Arc magma inferred from fractionation paths.

907   Journal of Petrology, 52, 257-278.

908   Plank, T., Kelley, K.A., Zimmer, M.M., Hauri, E.K., Wallace, P.J. (2013) Why do mafic

909   magmas contain ~4 wt% water on average? Earth and Planetary Science Letters, 364,

910   168-179.

911   Portnyagin, M., Hoernle, K., Plechov, P., Mirono, N., Khubunaya, S. (2007) Constraints

912   on mantle melting and composition and nature of slab components in volcanic arcs from

913   volatiles (H_2O, S, Cl, F) and trace elements in melt inclusions from the Kamtchatka Arc.

914   Earth and Planetary Science Letters, 255, 53-69.

915   Putirka, K.D., Perfit, M., Ryerson, F.J., Jackson, M.G. (2007) Ambient and excess mantle

916   temperatures, olivine thermometry, and active vs. passive upwelling. Chemical Geology,

917   241, 177-206.

918   Putirka, K.D. (2008) Thermometers and barometers for volcanic systems. Reviews in

919   Mineralogy and Geochemistry, 69, 61-120.

920   Putirka, K., Ryerson, F.J., Perfit, M., Ridley, W.I. (2011) Mineralogy and composition of

921   the oceanic mantle. Journal of Petrology, 52, 279-313.

922   Righter, K., and Carmichael, I.S.E. (1996) Phase equilibria of phlogopite lamprophyres

923   from western Mexico: biotite-liquid equilibria and P-T estimates for biotite-bearing

924   igneous rocks. Contributions to Mineralogy and Petrology, 123, 1-21.

925   Roeder, P.L., and Emslie, R.F. (1970) Olivine-liquid equilibrium. Contributions to

926   Mineralogy and Petrology, 29, 275-289.

927   Ruscitto, D.M., Wallace, P.J., Johnson, E.R., Kent, A.J.R., Bindeman, I.N. (2010)

928   Volatile contents of mafic magmas from cinder cones in the Central Oregon High

929   Cascades: implications for magma formation and mantle conditions in a hot arc. Earth

930   and Planetary Science Letters, 298, 253-161.

931   Ruscitto, D.M., Wallace, P.J., Kent, A.J.R. (2011) Revisiting the compositions and

932   volatile contents of olivine-hosted melt inclusions from the Mount Shasta region:

933   implications for the formation of high-Mg andesites. Contributions to Mineralogy and

934   Petrology, 162, 109-132.

935   Sadofsky, S. J., Portnyagin, M., Hoernle, K., van den Bogaard, P. (2008) Subduction

936   cycling of volatiles and trace elements through the Central American volcanic arc:

937   evidence from melt inclusions. Contributions to Mineralogy and Petrology, 155, 433-456.

938   Shaw, A.M., Hauri, E.H., Fischer, T.P., Hilton, D.R., Kelley, K.A. (2008) Hydrogen

939   isotopes in Mariana arc melt inclusions: implications for subduction dehydration and the

940   deep-Earth water cycle. Earth and Planetary Science Letters, 275, 138-145.

941   Sisson, T.W., and Layne, G.D. (1993) H_2O in basalt and basaltic andesite glass inclusions

942   from four seduction-related volcanoes. Earth and Planetary Science Letters, 117, 619-

943   635.

944   Sisson, T.W., and Grove, T.L. (1993a) Experimental investigations of the role of H_2O in

945   calc-alkaline differentiation and subduction zone magmatism. Contributions to

946   Mineralogy and Petrology, 113,143-166.

947   Sisson, T.W., and Grove, T.L. (1993b) Temperatures and H_2O contents of low-MgO

948   high-alumina basalts. Contributions to Mineralogy and Petrology, 113, 167-184.

949   Snyder, D.A., and Carmichael, I.S.E. (1992) Olivine-liquid equilibria and the chemical

950   activities of FeO, NiO, Fe_2O_3, and MgO in natural basic melts. Geochimica et

951   Cosmochimica Acta, 56, 303–318.

952   Sobolev, A.V., Asafov, E.V., Gurenko, A.A., Arndt, N.T., Batanova, V.G., Portnyagin,

953   M.V., Garbe-Schönberg, E., Krasheninnikov, S.P. (2016) Komatiites reveal a hydrous

954   Archaean deep-mantle reservoir. Nature, 531, 628-632.

955   Stefano, C.J., Mukasa, S.B., Andronikov A., Leeman, W.P. (2011) Water and other

956   volatile systematics of olivine-hosted melt inclusions from Yellowstone hotspot track.

957   Contributions to Mineralogy and Petrology, 161, 615-633.

958   Takahashi, E. (1978) Partitioning of Ni^{2+}, Co^{2+}, Fe^{2+}, Mn^{2+} and Mg^{2+} between olivine and

959   silicate melts: compositional dependence of partition coefficient. Geochimica et

960   Cosmochimica Acta, 42, 1829–1844.

961   Tuff, J., Takahashi, E., Gibson, S.A. (2005) Experimental constraints on the role of

962   garnet pyroxenite in the genesis of high-Fe mantle plume derived melts. Journal of

963   Petrology, 46, 2023-2058.

964   Wade, J.A., Plank, T., Melson, W.G., Soto, G.J., Hauri, E. (2006) The volatile content of

965   magmas from Arenal volcano. Journal of Volcanology and Geothermal Research, 157,

966   94-120.

967   Wagner, T.P., Donnelly-Nolan, J.M., Grove, T.L. (1995) Evidence of hydrous

968   differentiation and crystal accumulation in the low-MgO, high Al_2O_3 Lake Basalt from

969   Medicine Lake volcano, California. Contributions to Mineralogy and Petrology, 121,

970   201-216.

971   Walker, J.A., Roggensack, K., Patino, L.C., Cameron, B.I., Matias, O. (2003) The water

972   and trace element contents of melt inclusions across an active subduction zone.

973   Contributions to Mineralogy and Petrology, 146, 62-77.

974   Wang, Z., and Gaetani, G.A. (2008) Partitioning of Ni between olivine and siliceous

975   eclogite partial melt: experimental constraints on the mantle source of Hawaiian basalts.

976   Contributions to Mineralogy and Petrology, 156, 661–678.

977   Waters, L.E., and Lange, R.A. (2013) Crystal-poor, multiply saturated rhyolites

978   (obsidians) from the Cascades and Mexican arcs: evidence of degassing-induced

979   crystallization of phenocrysts. Contributions to Mineralogy and Petrology, 166, 731-754.

980   Waters, L.E., and Lange, R.A. (2015) An updated calibration of the plagioclase-liquid

981   hygrometer-thermometer applicable to basalts through rhyolites. American Mineralogist,

982   100, 2172-2184.

983   Waters, L.E., Andrews, B.J., Lange, R.A. (2015) Rapid crystallization of plagioclase

984   phenocrysts in silicic melts during fluid-saturated ascent: phase equilibrium and

985   decompression experiments. Journal of Petrology, 56, 981-1006.

986 Welsch, B., Hammer, J., Hellebrand, E. (2014) Phosphorus zoning reveals dentritic

987 architecture of olivine. Geology, 42, 867-870.

988 Xu, G., Huang, S., Frey, F.A., Blichert-Toft, J., Abouchami, W., Clague, D.A., Cousens,

989 B., Moore J., Beeson, M.H. (2014) The distribution of geochemical heterogeneities in the

990 source of Hawaiian shield lavas as revealed by a transect across the strike of the Loa and

991 Kea spatial trends: East Molokai to West Molokai to Penguin Bank. Geochimica et

992 Cosmocimica Acta, 132, 214-237.

993 Zhang, Y., Xu, Z., Zhu, M., Wang, H. (2007). Silicate melt properties and volcanic

994 eruptions. Reviews of Geophysics, 45, RG4004.

995 Zimmer, M.M., Plank, T., Hauri, E.H., Yogodzinksi, G.M., Stelling, P., Larsen, J.,

996 Singer. B., Jicha, B., Mandeville, C., Nye, C.J. (2010) The role of water in generating the

997 calc-alkaline trend: new volatile data for Aleutian magmas and a new tholeiitic index.

998 Journal of Petrology, 51, 2411-2444.

999
1000

1001   **FIGURE CAPTIONS**

1002

1003   **FIGURE 1.** (a) Plot of $T_{expt} - T_{Ni}$ (temperature calculated from Ni-thermometer; Eq.1,

1004   Table 3) for the 123 olivine-melt experiments in Appendix B; (b) same as (a), but for

1005 $T_{expt}-T_{Mg}$ (temperature calculated from Mg-thermometer; Eq. 1, Table 3); (c) same as (a),

1006   but $\Delta T = T_{Mg}-T_{Ni}$ (difference in calculated temperature from the Mg-thermometer and Ni-

1007   thermometer). The results show no systematic difference between the two thermometers

1008   over a wide range of temperature and anhydrous melt composition (Appendix B). The

1009   solid squares are results from the hydrous olivine-melt equilibrium experiments of Moore

1010   and Carmichael (1998; Table 7) and show that the Ni-thermometer more accurately

1011   recovers experimental temperatures under hydrous conditions than the Mg-thermometer.

1012

1013   **FIGURE 2.** Open and solid circles are the difference between the experimental

1014   temperatures of Matzen et al. (2013) and the temperatures calculated from the Mg-

1015   thermometer and Ni-thermometer (Eq. 1 and Table 3), respectively, for each olivine-melt

1016   equilibrium experiment from Matzen et al. (2013). The solid line shows the Herzberg

1017   and O'Hara (2002) pressure correction (Eq. 2 in text); the solid line closely matches the

1018   the difference in the experimental temperatures of Matzen et al. (2013) and the

1019   temperature calculated from the Mg-thermometer in this study. The dashed line is a

1020   linear fit to the solid circles between 0 and 1 GPa (slope is 4°C/GPa) and shows that the

1021   Ni-thermometer has a negligible pressure correction over this interval. However, the Ni-

1022   thermometer has a strong dependence on pressure at ≥ 2 GPa. The step-wise behavior for

1023   the Ni-thermometer between 1bar to 3 GPa is explained in the text.

46

1024

1025

1026   **FIGURE 3.** Plot of ΔT (=T_{Mg}-T_{Ni}) values for nine MORB samples (open triangles;

1027   Table 5) and 18 subduction-zone lavas (solid squares; Table 6). T_{Mg} and T_{Ni} are obtained

1028   from the Mg-thermometer and Ni-thermometer, respectively (Eq. 1; Table 3). Also

1029   shown are ΔT values for the 123 1-bar experiments in Appendix B up to 1350°C (gray

1030   circles). The MORBs have ΔT values that fall within the range of those for the

1031   experiments in Appendix B, whereas the subduction-zone samples have ΔT values that

1032   are systematically larger (and always positive) relative to the MORBs and the anhydrous

1033   experiments. It is hypothesized that the reason why the subduction-zone samples have

1034   large, positive ΔT values is because the Ni-thermometer more accurately calculates the

1035   temperature of olivine crystallization in a hydrous melt (and does not require a correction

1036   for H_2O in the melt), whereas the Mg-thermometer overestimates the temperature if a

1037   separate correction for H_2O in the melt is not applied.

1038

1039   **FIGURE 4.** Plots of wt% NiO vs. mol% Fo (= XMgO/(XMgO+XFeO) x 100) for the

1040   most Mg-rich olivine analyses (highest 3 mol% Fo) in each of the 18 subduction-zone

1041   samples from the Mexican arc (Table 6).   A linear fit to the data (equation in each plot)

1042   enables calculation of wt% NiO in the most Fo-rich olivine analyzed in each sample

1043   (Table 6). This value of wt% NiO is used to apply the Ni-thermometer (Eq. 1; Table 3)

1044   to these 18 samples.

1045

47

1046   **FIGURE 5.** Plot of the difference in calculated temperatures from the Mg-thermometer

1047   in this study (Eq. 1 and Table 3; corrected for pressure with Eq. 2) and those from the

1048   Putirka et al. (2007) Mg-thermometer (which includes a correction for pressure and H_2O

1049   in the melt) applied to the hydrous experiments of Almeev et al. (2007) and Médard and

1050   Grove (2008), as a function of melt water content. The results illustrate that any

1051   thermometer based on $D_{Mg}^{ol/liq}$ requires a large correction for H_2O content in the melt.

1052

1053   **FIGURE 6.** Simplified phase diagram based on the phase-equilibrium experiments of

1054   Moore and Carmichael (1998) on a basaltic andesitic composition (MAS-22, Table 7)

1055   under pure-H_2O fluid-saturated conditions. (A more detailed figure in Appendix K

1056   shows the experimental results that constrain the placement of mineral-in curves.)

1057   Abbreviations in the plot: hbd (hornblende); oliv (olivine); plag (plagioclase); aug

1058   (augite). The dashed lines are isopleths of maximum H_2O solubility in the melt from the

1059   model in Zhang et al. (2007). A plausible adiabatic ascent path (arrow) is shown for

1060   APA-6 (intersects olivine-in curve at 1075 °C based on Ni-thermometry results; Table 6),

1061   which has a bulk composition similar to that for MAS-22 (Table 7). Shown on this

1062   ascent path is the maximum H_2O content of 3.9 wt% analyzed in olivine-hosted melt

1063   inclusions from scoria erupted from the same cinder cone as APA-6 (Cerro el Hungaro;

1064   Johnson et al., 2009). A plausible adiabatic ascent path for both NI-21 and UR-2, which

1065   have nearly identical bulk compositions, is also shown (intersects the olivine-in curve at

1066   ~1020 °C based on the Ni-thermometer results; Table 6). The absence of plagioclase

1067   phenocrysts in NI-21 is attributed to a more rapid fluid-saturated ascent relative to that

1068   for UR-2, leading to large effective under-coolings ($\Delta T_{eff} = T_{liquidus} - T_{melt}$) and a kinetic

1069   delay to the nucleation and growth of plagioclase phenocrysts (e.g., Waters et al., 2015).

1070   Both APA-6 and NI-21 contain olivine phenocrysts with diffusion-limited growth

1071   textures (Fig. 7), consistent with crystal growth under super-saturated (i.e. undercooled)

1072   conditions (see text for discussion).

1073

1074   **FIGURE 7.** Back-scattered electron (BSE) images of representative olivine phenocrysts

1075   in six of the subduction-zone samples in Table 6. In each case, the olivine phenocryst

1076   displays a hopper texture, which forms when the crystal grows rapidly under diffusion-

1077   limited conditions, which is consistent with large effective under-coolings ($\Delta T_{eff}=$

1078 $T_{liquidus}$-T_{melt}) caused by rapid H_2O degassing during magma ascent (e.g., Welsch et al.,

1079   2014).

1080

1081   **FIGURE 8.** Simplified phase diagram based on the phase-equilibrium experiments of

1082   Barclay and Carmichael (2004) on sample JOR-46 (scoria from the same cinder cone as

1083   JOR-46d; Luhr and Carmichael, 1985) under pure-H_2O fluid-saturated conditions. (A

1084   more detailed figure in Appendix K shows the experimental results that constrain the

1085   placement of mineral-in curves.) Abbreviations in the plot: hbd (hornblende); oliv

1086   (olivine); aug (augite). Dashed lines are isopleths of maximum H_2O solubility in the melt

1087   from the model in Zhang et al. (2007). A plausible adiabatic ascent path (arrow) is

1088   shown for JOR-46d, within the constraints of the Ni-thermometer (gray box; 1105 ± 29

1089   °C) for the onset of olivine crystallization and the experimentally constrained stability

1090   field for hornblende. JOR-46d is the only sample in Table 6 that contains hornblende in

1091   its phenocryst assemblage (Luhr and Carmichael, 1985).

49

1092

1093   **FIGURE 9.** Plot of wt% H_2O in the melt phase from 36 olivine-melt equilibrum

1094   experiments from the literature (Parman et al., 2011 - open circle; Médard and Grove,

1095   2008 - solid circle; Almeev et al., 2007 - open triangle; Berndt et al., 2005 - solid

1096   triangle; Moore and Carmicheal, 1998 - open diamond; Wagner et al., 1995 - solid

1097   diamond; Sisson and Grove, 1993a - empty square; Sisson and Grove, 1993b - solid

1098   square) plotted as a function of ΔT (= $T_{anhydrous}$-$T_{hydrous}$ = T_{Mg}-T_{expt}). The anhydrous

1099   temperature for each experiment is calculated using the Mg-thermometer (Eq. 1 and

1100   Table 3; corrected for pressure with Eq. 2), whereas the hydrous temperature is the

1101   reported experimental temperature. Run conditions for all 36 experiments are reported in

1102   Appendix L. The dashed curve is a second order polynomial equation (Eq. 6), which is a

1103   fit to the experiments at the bottom of the data cloud only. Equation 6 allows the

1104   minimum concentration of water in the melt to be calculated from ΔT (=$T_{anhydrous}$-

1105 $T_{hydrous}$).

1106
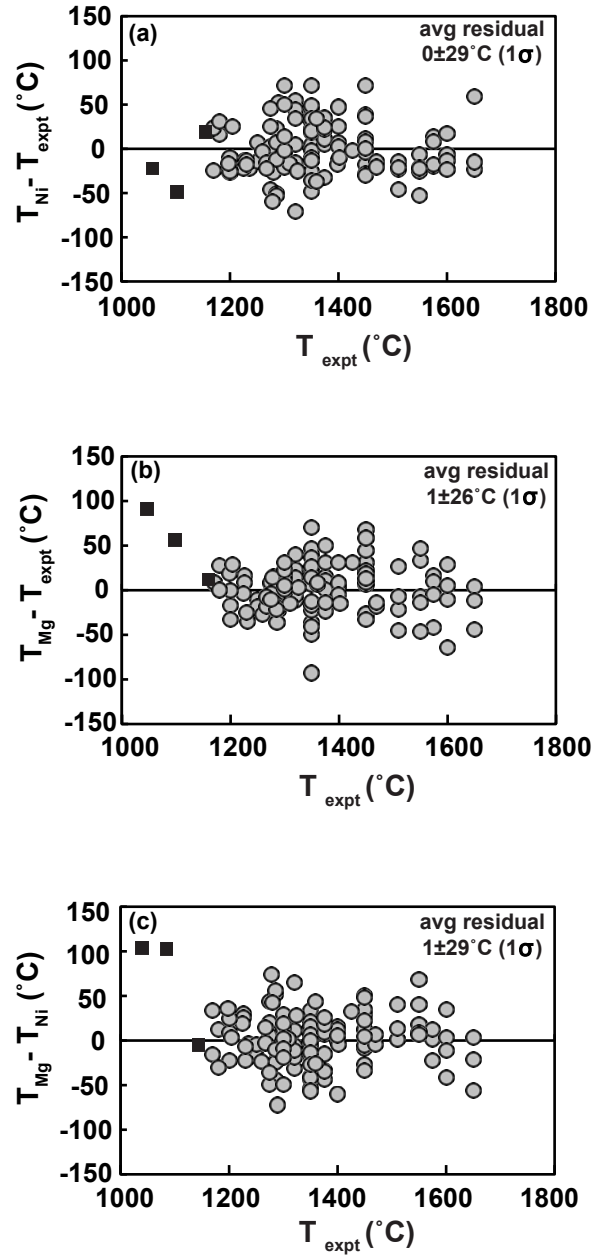
Figure 1

Figure 2
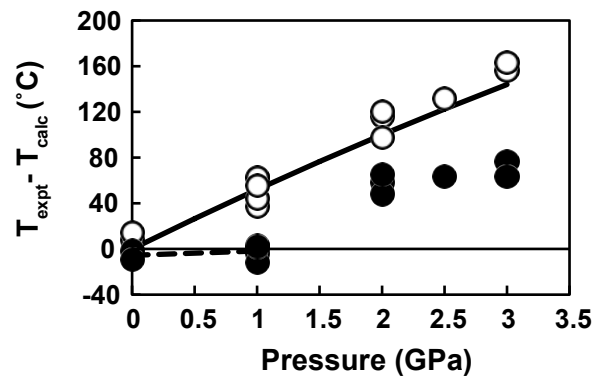
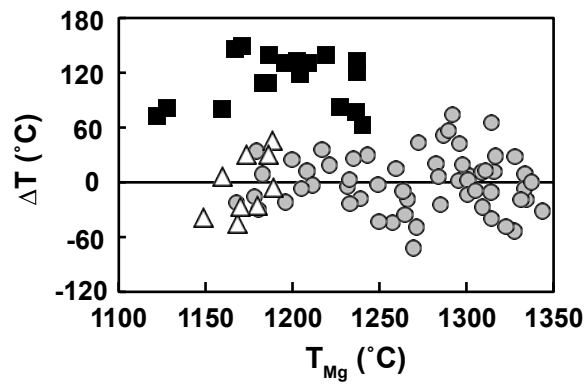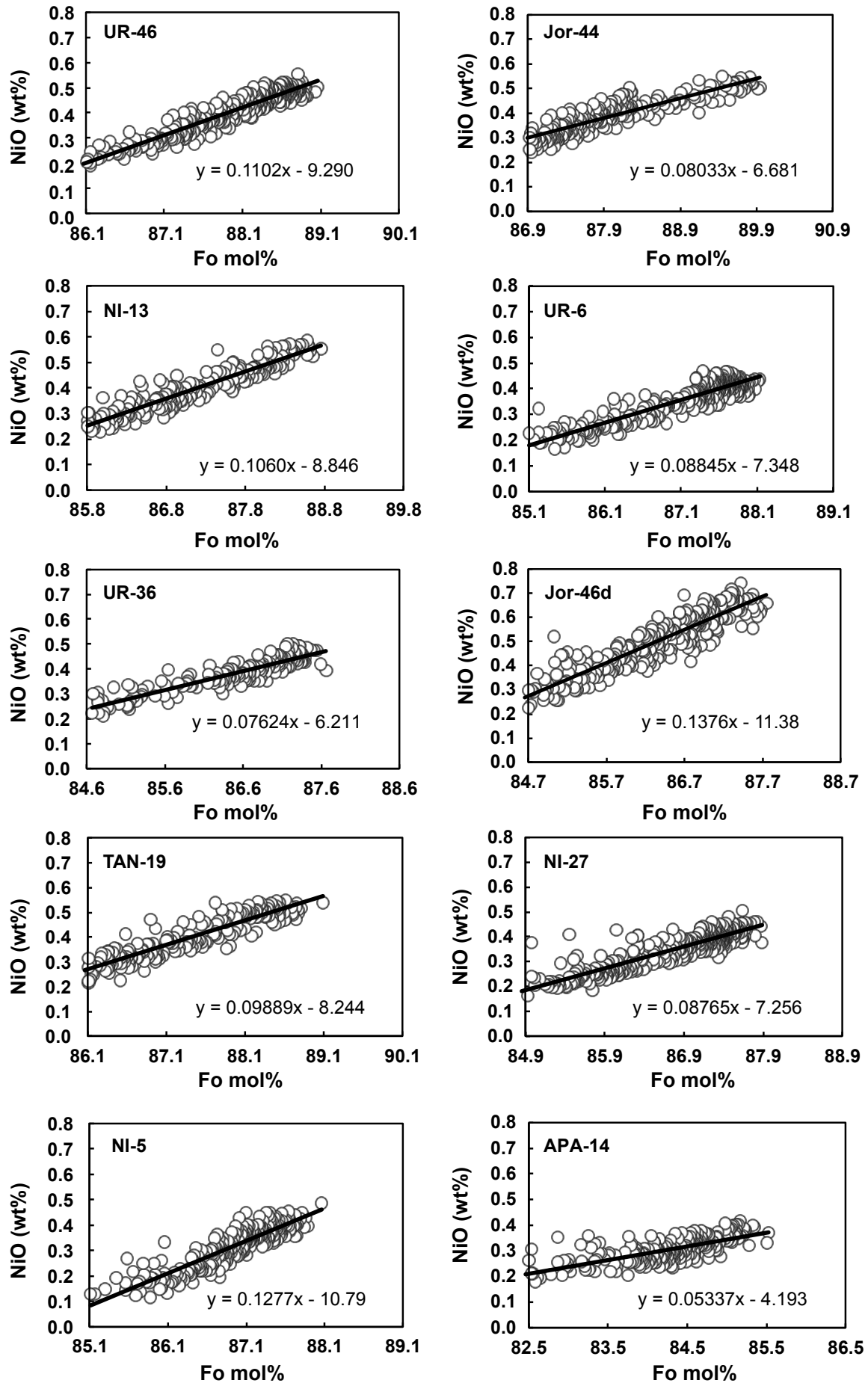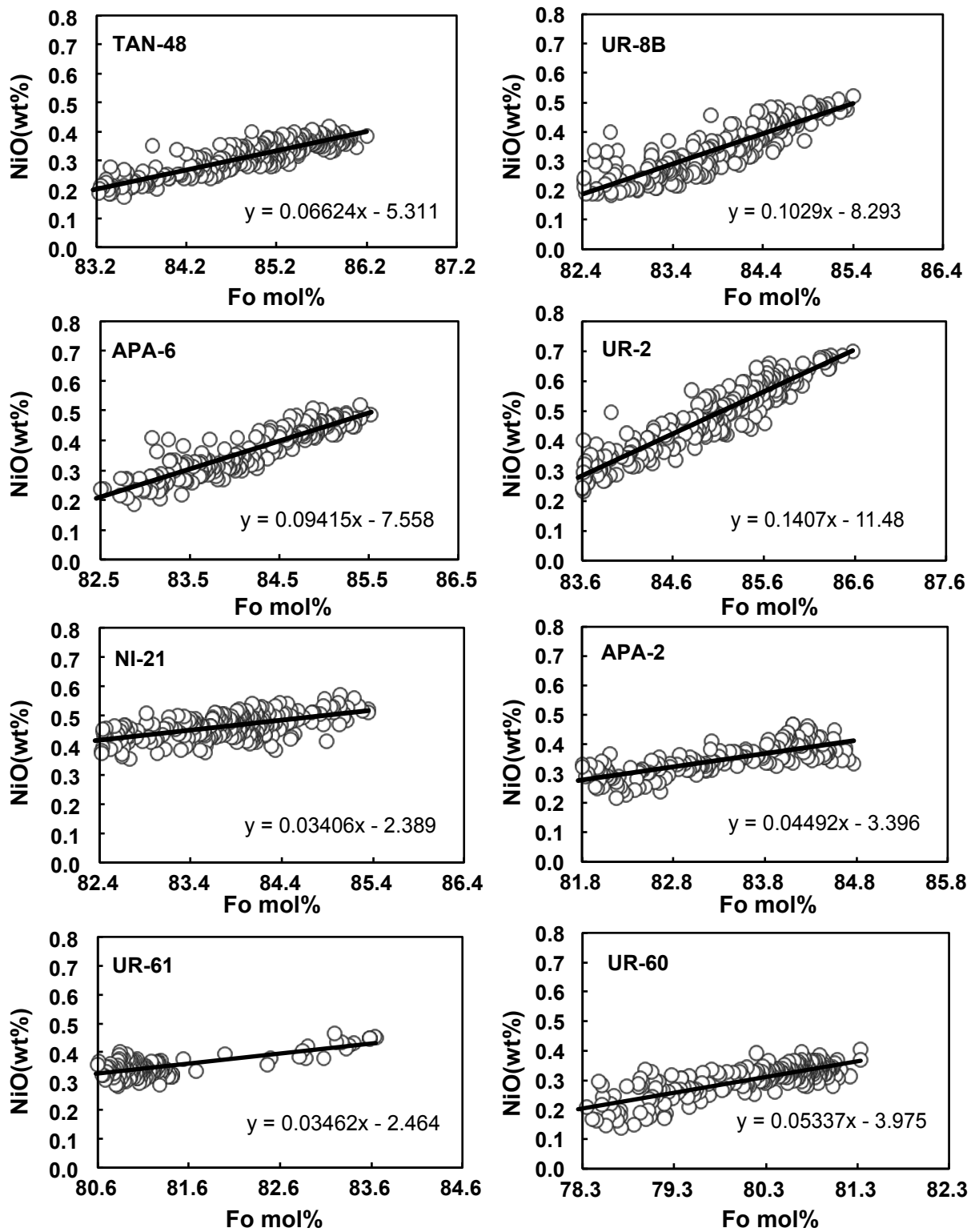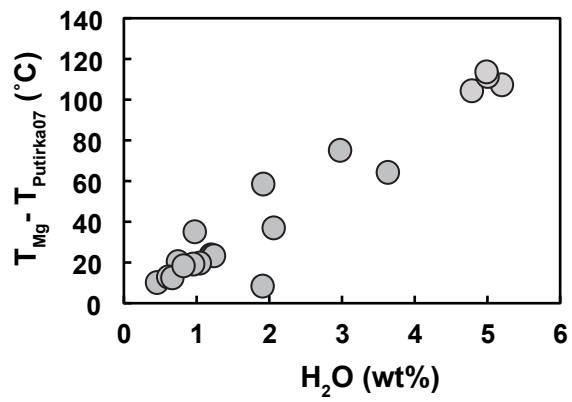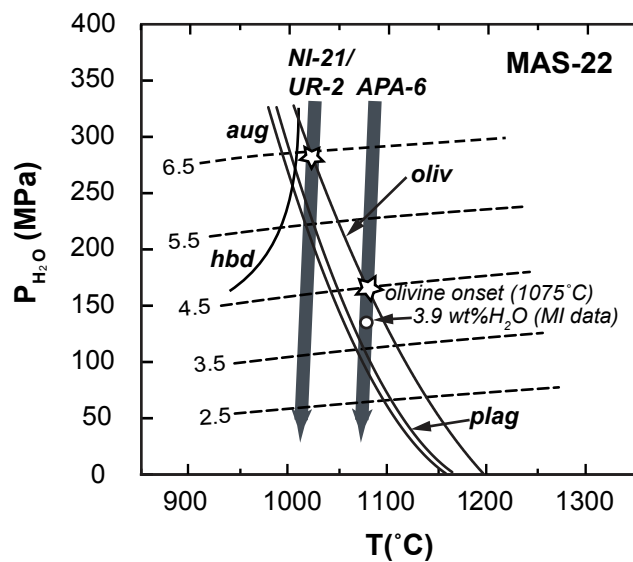Figure 3

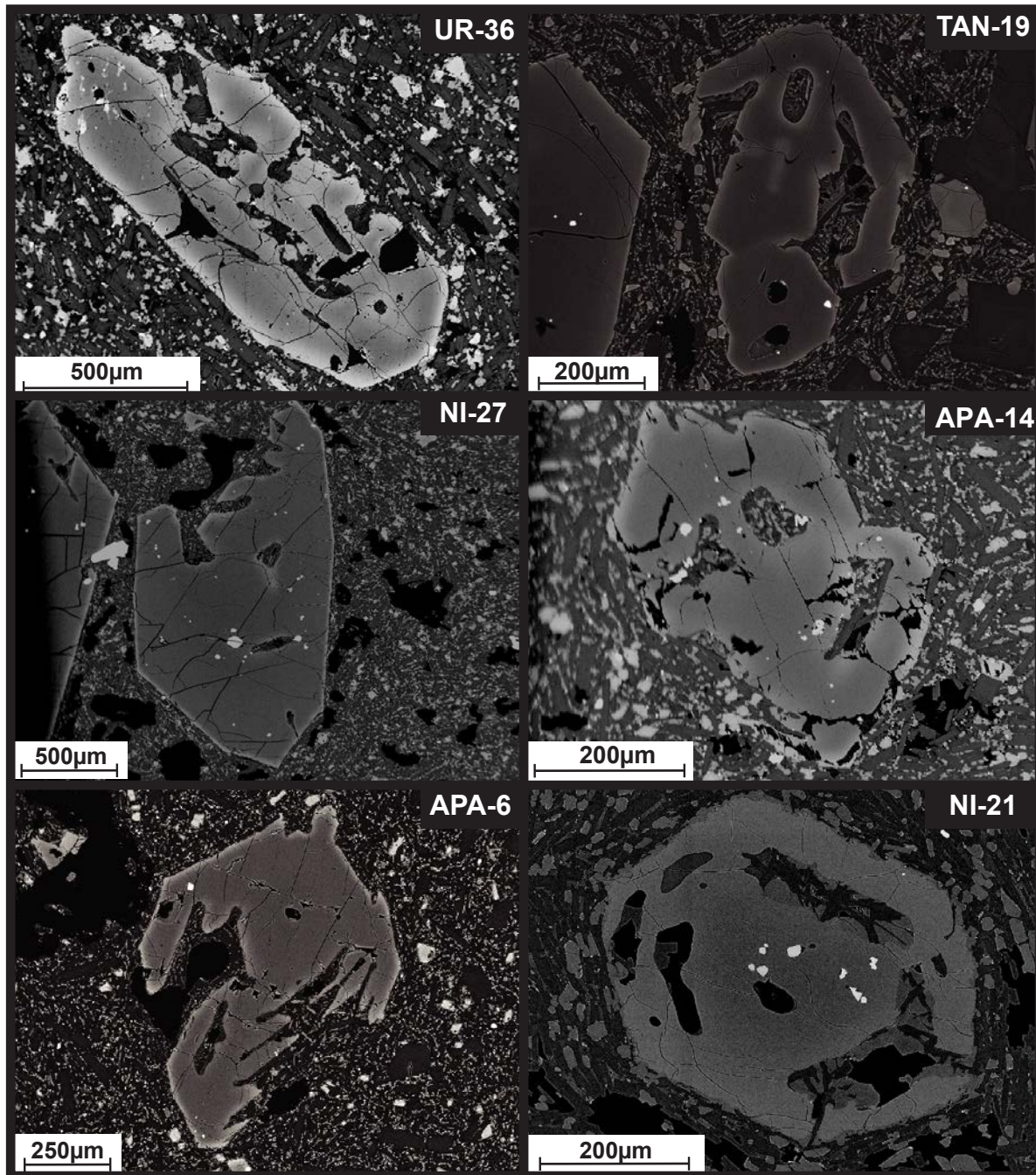Figure 4 page 1
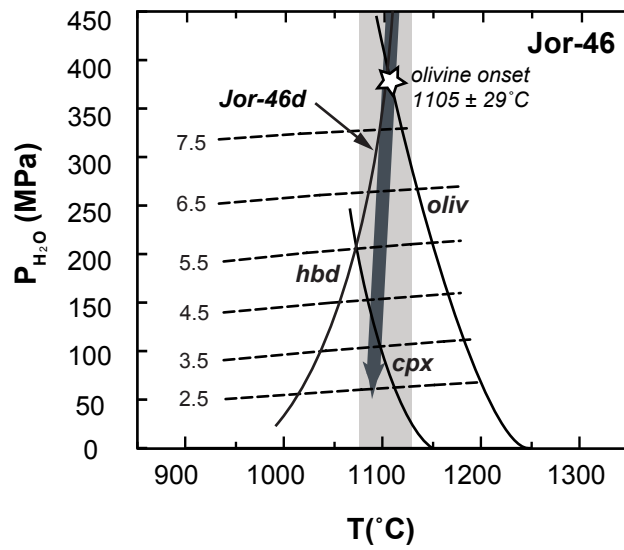
Figure 4 Page 2

Figure 5

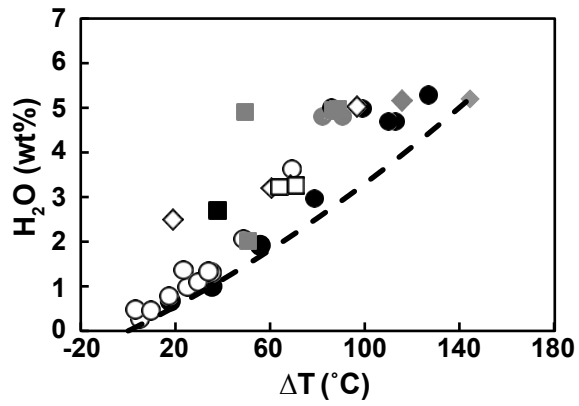Figure 6

Figure 7

Figure 8

Figure 9

Table 1. The equations and average residuals for 13 $D_{Ni}^{oliv/liq}$ models from the literature applied to data in Appendix B.

Studies		Rearranged Equations*	Average Residual ($\pm 1\sigma$)
Matzen et al., 2013		$T(K) = \dfrac{4338}{\ln D_{Ni}^{oliv/liq}(mol\%) - \ln D_{Mg}^{oliv/liq}(mol\%) + 1.956}$	19 ± 98 °C
Putirka et al., 2011	Eqn. 2a	$T(°C) = \dfrac{6800}{\ln D_{Ni}^{oliv/liq}(wt\%) + 3.257}$	-16 ± 70 °C
	Eqn. 2b	$T(°C) = \dfrac{6829}{\ln D_{Ni}^{oliv/liq}(wt\%) - 0.033 * SiO_2^{liq}(wt\%) + 4.75}$	58 ± 75 °C
	Eqn. 2c	$T(°C) = \dfrac{3236}{\ln D_{Ni}^{oliv/liq}(wt\%) - 0.04 * SiO_2^{liq}(wt\%) + 0.04 * MgO^{liq}(wt\%) + 1.78}$	144 ± 119 °C
	Eqn. 2c'	$T(°C) = \dfrac{3235.6}{\ln D_{Ni}^{oliv/liq}(wt\%) - 0.038 * SiO_2^{liq}(wt\%) + 0.045 * MgO^{liq}(wt\%) + 1.783}$	4 ± 49°C
Li and Ripley, 2010		$T(K) = \dfrac{9250}{\ln D_{Ni}^{oliv/liq}(wt\%) + 0.618 * (X_{FeO}^{liq} + X_{MgO}^{liq} + X_{MnO}^{liq} + X_{CaO}^{liq} + X_{CoO}^{liq} + X_{NiO}^{liq})/X_{SiO2}^{liq} + 4.02}$	-9 ± 30 °C
Wang and Gaetani, 2008		$T(K) = \dfrac{7100}{ln D_{Ni}^{oliv/liq}(wt\%) + 0.71 * \ln(NBO/T) + 2.5}$	-39 ± 75 °C
Keleman et al., 1998		$T(K) = \dfrac{15850}{\ln D_{Ni}^{oliv/liq}(wt\%) + 7.69}$	29 ± 54°C
Agee and Walker, 1990	SiO$_2$	$T(K) = \dfrac{10800}{\ln D_{Ni}^{oliv/liq}(wt\%) - 0.04 * SiO_2^{liq}(wt\%) + 6.66}$	60 ± 59°C
	MgO	$T(K) = \dfrac{93000}{D_{Ni}^{oliv/liq}(wt\%) + \dfrac{45}{MgO^{liq}(wt\%)} + 45}$	40 ± 86°C
Hart and Davis, 1978		$T(K) = \dfrac{12345}{\ln D_{Ni}^{oliv/liq}(wt\%) + 5.593}$	30 ± 57°C
Leeman and Lundstrom, 1978	wt%	$T(K) = \dfrac{13376}{\ln D_{Ni}^{oliv/liq}(wt\%) + 6.34}$	3 ± 54°C
	mole%	$T(K) = \dfrac{14298}{\ln D_{Ni}^{oliv/liq}(mole\%) + 6.99}$	15 ± 54°C
Arndt, 1977		$T(K) = \dfrac{10430}{\ln D_{Ni}^{oliv/liq}(mole\%) + 4.79}$	-17 ± 60°C

Notes:

All the models were originally fit with $\ln D_{Ni}$ or D_{Ni} as the dependent variable. They were rearranged to calculate temperature from analyzed D_{Ni} and melt compositions.

Eqn. 2c' is Eqn. 2c from Putirka et al. (2011) with one more significant digit on each of the fit parameters than what is reported (determined by trial and error to obtain a better residual for the 123 experiments).

Table 2. The average residual for eight model equations (from Table 1) re-calibrated on the 123 1-bar experiments in Appendix B.

Studies	Rearranged Equations	Average $T_{calc} - T_{expt}$ (with 1σ)	R^2
Model A	$T(K) = 9090(\pm24))/ (\ln D_{Ni}^{oliv/liq}(wt\%) + 0.677\ (\pm0.026)$ $* (X_{FeO}^{liq} + X_{MgO}^{liq} + X_{MnO}^{liq} + X_{CaO}^{liq} + X_{CoO}^{liq} + X_{NiO}^{liq})/X_{SiO2}^{liq} + 3.904\ (\pm0.147))$	-1 ± 31 ˚C	0.961
Model B	$T(K) = 6902\ (\pm35)/(\ln D_{Ni}^{oliv/liq}(wt\%) - 0.029\ (\pm0.001) * (SiO_2^{liq}(wt\%) - MgO^{liq}(wt\%)) +$ $3.442\ (\pm0.189))$	-1 ± 49 ˚C	0.942
Model C	$T(K) = 12958(\pm373)/(\ln D_{Ni}^{oliv/liq}(wt\%) - 0.0371\ (\pm0.0025) * SiO_2^{liq}(wt\%) + 8.042\ (\pm0.298)$	1 ± 33 ˚C	0.911
Model D	$T(K) = 7965\ (\pm48)/(\ln D_{Ni}^{oliv/liq}(wt\%) + 0.492(\pm0.041)) * (NBO/T) + 2.957\ (\pm0.295)$	2 ± 60 ˚C	0.863
Model E	$T(K) = 17841\ (\pm871)/(\ln D_{Ni}^{oliv/melt}(mol\%) + \ln D_{Mg}^{oliv/melt}(mol\%) + 8.254\ (\pm0.535))$	2 ± 56 ˚C	0.776
Model F	$T(K) = 10517(\pm560)/(\ln D_{Ni}^{oliv/liq}(mol\%) + 4.768(\pm0.344))$	-3 ± 61˚C	0.745
Model G	$T(K) = 11070\ (\pm592)/(\ln D_{Ni}^{oliv/liq}(wt\%) + 4.946\ (\pm0.363))$	3 ± 62˚C	0.743
Model H	$T(K) = 66644\ (\pm5083)/(D_{Ni}^{oliv/liq}(wt\%) - 1/MgO^{liq}(wt\%) + 33.745 \pm 3.118)$	4 ± 83˚C	0.696

Model A is based on the Li and Ripley (2010) model.
Model B is based on Eq. 2c in Putirka et al. (2011).
Model C is based on Eq. 2b in Putirka et al. (2011) and the SiO$_2$ model in Agee and Walker (1990).
Model D is based on the Wang and Gaetani (2008) model.
Model E is based on the Matzen et al. (2013) model.
Model F is based on the mole% model in Leeman and Lundstrom (1978) and the model in Arndt (1977),
Model G is based on Eq. 2a in Putirka et al. (2011), Leeman and Lundstrom (1978), Keleman et al. (1998), and Hart and Davis, (1978).
Model H is based on the MgO equation in Agee and Walker (1990).
$\ln D_{Ni}$ or D_{Ni} was the dependent variable in all fits, except $D_{Ni} - 1/MgO$ for Model H, and $\ln D_{Ni} + \ln D_{Mg}$ for Model E.

Table 3. Fitted parameters and statistics for calibration of Eqn.1 for Ni and Mg

	T_{Ni}	T_{Mg}
fitted value ± 1σ		
a	-4.32 ± 0.33	-4.74 ± 0.20
b	9416 ± 296	6701 ± 182
c	-0.71 ± 0.13	-1.12 ± 0.08
d	0.53 ± 0.24	-1.08 ± 0.15
e	0.35 ± 0.11	0.64 ± 0.07
statistics		
SEE	29	26
R^2	0.96	0.96

Table 4. The average residuals for the Mg-thermometers of Beattie (1993) and Putirka et al. (2007) re-calibrated on the 123 experiments in Appendix B.

Studies	Equations	Average Residual (with 1σ)
Beattie, 1993	$$T(K) = \frac{13603.6 + 4.943 * 10^{-7} * (P(Pa) - 10^5)}{6.26 + 2 * lnD\left(Mg_{Mg}^{oliv/liq}\right) + 2\,ln\left(1.5 * C_{NM}^{liq}\right) + 2 * ln(3 * C_{SiO2}^{liq}) - NF}$$	17 ± 30 ˚C
Putirka et al., 2007	$$T(°C)$$ $$= \frac{15294.6 + 1318.8 * P(GPa) + 2.4834 * P(GPa)^2}{8.048 + 2.8352 * lnD_{Mg}^{oliv/liq} + 2.097 * ln\left(1.5 * C_{NM}^{liq}\right) + 2.575 * ln\left(3 * C_{SiO2}^{liq}\right) - 1.41 * NF + 0.222 * H2O^{Liq} + 0.5 * P(GPa)}$$	0 ± 31˚C

Table 5. Compositions and modes for MORB samples reported in Allan et al. (1989); temperatures from this study

Sample Name	F9-1	1570-1949	1572-1755-2	1559-2058	1567-1816	F1-1	1562-1941	1569-1901	F7-4
melt (glass) composition									
SiO_2 (wt%)	49.6	49.42	48.96	49.49	50.06	50.41	49.04	50.31	50.52
TiO_2 (wt%)	1.21	0.96	1.14	1.08	1.16	1.18	1.55	1.18	1.54
Al_2O_3 (wt%)	16.9	16.6	16.9	16.1	16.2	15.5	16.6	14.4	14.3
FeO^T (wt%)	8.59	8.83	8.84	9.21	8.82	9.3	9.44	10.55	11.02
MgO (wt%)	8.97	8.78	8.51	8.30	8.28	8.14	7.80	7.56	7.05
CaO (wt%)	12.4	12.7	12.3	13.0	12.5	13.0	11.2	12.9	12.2
Na_2O (wt%)	2.46	2.43	2.71	2.51	2.46	2.41	2.84	2.47	2.87
K_2O (wt%)	0.10	0.04	0.06	0.04	0.11	0.06	0.04	0.07	0.09
P2O5 (wt%)	0.10	0.08	0.13	0.10	0.14	0.11	0.17	0.11	0.14
Ni (ppm)	189	140	142	72	162	124	106	55	80
Total	100.23	99.81	99.51	99.85	99.71	100.10	98.62	99.59	99.76
phenocryst (ph) information									
oliv ph(vol%)	0.4	0.1[a]	0.4	0.5[a]	0.3	0.5	0.2	0.1	0.1
plag ph (vol%)	0.0	0.5	0.6	0.8	1.0	2.0	1.1	0.7	3.4
cpx ph (vol%)	0.0	0.0	0.0	0.0	0.0	0.0	0.0	0.2	2.2
total (vol%)	0.4	0.5	1.0	0.8	1.3	2.5	1.3	1.0	5.7
max. Fo content in olivine	90.6	88.0	87.8	87.5	86.9	86.6	86.1	83.5	82.1
olivine NiO (wt%)	0.4	0.23	0.28	0.15	0.26	0.19	0.18	0.11	0.14
$D_{Ni}^{oliv/liq}$	16.5	13.0	15.6	16.6	12.8	12.3	13.6	15.8	14.2
calculated temperature and H_2O									
T_{Mg} (°C)	1188	1189	1186	1173	1180	1168	1170	1160	1149
T_{Ni} (°C)	1143	1194	1156	1143	1205	1214	1196	1153	1187
ΔT $(T_{Mg}-T_{Ni})$[b]	45	-5	30	31	-25	-45	-27	6	-39

a. olivine crystals ≤ 250 microns (in other cases only crystals ≥ 250 micron are counted).
b. The average ΔT value for the 9 samples is -3 degrees, which indicates a minimum melt water content of 0 wt% using Eq. 6

Table 6. Compositions and modes for 18 samples from the Mexican arc reported in Ownby et al. (2010) and Luhr and Carmichael (1985); temperatures from this study

sample name	UR-46	Jor-44	NI-13	UR-6	UR-36	Jor-46d	TAN-19	NI-27	NI-5	APA-14	TAN-48	UR-8B	APA-6	UR-2	NI-21	APA-2	UR-61	UR-60
Whole-rock composition																		
SiO_2 (wt%)	52.2	52.1	53.7	53.5	52.3	51.72	54.5	54.0	53.2	52.7	53.9	55.0	56.0	56.9	57.3	56.2	59.4	58.9
TiO_2 (wt%)	0.8	0.81	0.87	0.91	0.96	1.22	0.83	0.81	1.28	1.14	1.13	1.07	0.88	0.78	0.85	0.93	0.80	0.80
Al_2O_3 (wt%)	16.7	16.4	16.7	16.9	17.1	15.1	17.2	17.6	15.2	17.5	17.1	16.1	17.6	17.7	17.3	17.4	17.2	17.8
FeO^T (wt%)	7.39	7.45	7.20	7.46	7.76	7.32	6.82	7.08	7.00	7.89	7.44	7.13	6.69	6.36	6.26	6.73	5.87	5.83
MnO (wt%)	0.13	0	0.12	0.13	0.13	0.12	0.12	0.12	0.12	0.14	0.13	0.12	0.11	0.11	0.11	0.12	0.10	0.11
MgO (wt%)	9.38	9.29	8.98	8.62	8.52	8.03	7.92	7.68	7.59	7.46	7.04	6.52	6.35	5.87	5.83	5.70	4.31	4.27
CaO (wt%)	9.26	8.46	7.99	8.27	8.7	7.45	7.98	8.23	8.84	8.60	8.36	7.76	7.28	7.12	7.06	7.56	6.71	6.67
Na_2O (wt%)	3.37	3.47	3.33	3.37	3.52	4.55	3.68	3.59	3.19	3.60	3.76	4.06	3.84	3.95	3.96	3.77	4.03	3.93
K_2O (wt%)	0.56	0.74	0.89	0.67	0.79	2.54	0.77	0.65	2.88	0.71	0.89	1.66	1.07	0.97	1.10	1.28	1.40	1.51
P_2O_5 (wt%)	0.14	0.14	0.18	0.19	0.18	0.9	0.18	0.15	0.68	0.24	0.28	0.50	0.23	0.20	0.23	0.26	0.25	0.25
Ni (ppm)	231	261	201	178	145	221	156	130	124	100	110	108	120	122	90	100	77	65
Total	99.9	98.9	100.0	100.0	100.0	99.0	100.0	99.9	100.0	100.0	100.0	99.9	100.1	100.0	100.0	100.0	100.1	100.1
Phenocryst (ph) information																		
olivine ph[a] (vol%)	5.1	5.8	8.6	5.8	6.7	8.3	6.1	4.8	2.9	3.6	4.4	4.2	3.5	5.2	3.9	5.7	1.5	0.5
plagioclase ph[a] (vol%)	0.0	0	0.0	0.0	0.0	0.0	3.7	0.5	0.0	0.0	0.7	0.0	0.0	5.1	0.0	0.6	0.4	0.7
clinopyroxene pht[a] (vol%)	0.0	0	0.0	2.0	0.0	0.2	0.0	0.0	0.6	0.0	0.0	0.0	0.0	0.0	0.0	0.0	0.0	0.7
total ph (vol%)	5.1	5.8	8.6	7.8	6.7	8.5	9.8	5.3	3.5	3.6	5.1	5.8	3.5	10.3	3.9	6.3	1.9	1.9
Olivine composition, calculated Fe^{3+}/Fe^T and ΔNNO																		
max. Fo content[b]	89.1	89.9	88.8	88.1	87.7	87.7	89.1	87.9	88.1	85.5	86.2	85.4	85.5	86.6	85.4	84.8	83.6	81.3
Fe^{3+}/Fe^T (KD=0.34)	0.19	0.27	0.17	0.18	0.19	0.19	0.25	0.21	0.23	0.16	0.21	0.18	0.16	0.25	0.17	0.21	0.24	0.12
[c]ΔNNO (KD=0.34)	-0.2	0.8	-0.4	-0.2	-0.1	-0.2	0.6	0.2	0.3	-0.6	0	-0.3	-0.7	0.6	-0.5	0.0	0.2	-1.5
Fe^{3+}/Fe^T (KD=0.37)	0.25	0.32	0.24	0.25	0.26	0.26	0.32	0.27	0.29	0.23	0.27	0.25	0.24	0.31	0.23	0.27	0.31	0.19
[c]ΔNNO (KD=0.37)	0.6	1.3	0.5	0.6	0.7	0.7	1.4	0.9	1.1	0.3	0.8	0.6	0.5	1.2	0.4	0.8	1.2	-0.2
olivine NiO (wt%)[d]	0.53	0.54	0.57	0.44	0.48	0.69	0.57	0.45	0.46	0.37	0.40	0.49	0.49	0.70	0.52	0.41	0.43	0.37
$D_{Ni}^{oliv/liq}$	17.3	16.3	22.3	19.9	26.0	21.9	26.7	27.8	28.5	31.4	27.9	35.7	32.1	43.8	47.1	33.8	45.4	43.5
Calculated temperature and minimum wt% H_2O																		
T_{Mg} (°C)	1236	1240	1237	1227	1219	1237	1209	1204	1202	1195	1186	1186	1183	1167	1171	1159	1122	1128
T_{Ni} (°C)	1159	1177	1117	1145	1079	1105	1078	1086	1069	1065	1077	1047	1075	1020	1021	1079	1050	1046
ΔT (T_{Mg}-T_{Ni})[e]	78	63	120	82	140	133	130	118	133	131	109	140	108	147	150	81	72	82
minimum wt% H_2O[f]	2.4	1.9	4.2	2.6	5.0	4.7	4.6	4.1	4.7	4.6	3.7	5.0	3.6	5.3	5.5	2.6	2.3	2.6

a. phenocryst are crystals ≥300μm.
b. Fo =XMgO/(XMgO+XFeO)*100; the Fo content from olivine stoichiometry (XMgO/(XMgO+XFeO+XMnO+XCaO+XNiO)) in Appendix H
c. calculated with Eq. 12 in Jayasuriya et al. (2004).
d. calculated for max Fo olivine from linear fits in Fig. 4.
e. the average ΔT of 18 samples is 112 degrees.
f. minimum H2O calculated based on Eq.6; average of 18 samples is 3.8 wt%.

Table 7. Compositions and experimental conditions for three experiments reported in Moore and Carmichael (1998); temperatures from this study

Sample	MAS-22[a]	Expt 22-7	Expt 22-2	Expt 22-12
Melt composition[b]				
SiO_2 (wt%)	55.25	55.9	56.25	57.31
TiO_2 (wt%)	0.74	0.71	0.82	0.7
Al_2O_3 (wt%)	17.4	19.1	18.7	19.4
FeO^T (wt%)	5.98	5.77	5.40	4.94
MgO (wt%)	6.68	5.70	5.65	5.75
CaO (wt%)	7.28	6.68	7.31	7.08
Na_2O (wt%)	3.97	4.87	4.62	3.43
K_2O (wt%)	1.18	1.29	1.27	1.44
Ni (ppm)[c]	106	82.0	53.0	40.0
Total	98.49	100.02	100.00	100.05
Olivine composition[d]				
olivine Fo#[e]	-	85.4	88.1	95.2
olivine NiO (wt%)	-	0.23	0.27	0.24
$D_{Ni}{}^{oliv/liq}$	-	22.0	40.0	47.1
% olivine[f]	-	1.4	2.6	3.6
Experimental conditions and thermometry results				
ΔNNO	-	2.2	2.6	5.6
$P(H_2O)$ (MPa)	-	73.1	107.2	208.2
Expt. T(°C)	-	1150	1100	1050
H_2O (wt%)[g]	-	2.5	3.1	5.0
T_{Mg} (°C)	-	1165	1155	1136
$T_{Mg} - T_{expt}$ (˚C)	-	15	55	86
T_{Ni} (°C)	-	1174	1050	1029
$T_{Ni} - T_{expt}$ (˚C)	-	24	-50	-21

Notes:

a. whole-rock composition (Lange and Carmichael, 1990)

b. experimental glass compositions normalized to 100% anhydrous

c. measured in this study by laser ablation ICP-MS

d. measured in this study by electron microprobe

e. Fo # = XMgO/(XMgO+XFeO)*100;

f. calculated from Eq. 5 in text.

g. calculated from Zhang et al. (2007) water solubility model.